PNAS
www.pnas.org

Supplementary Information for

# Direct field evidence of autocatalytic iodine release from atmospheric aerosol

Yee Jun Tham[a], Xu-Cheng He[a], Qinyi Li[b], Carlos A. Cuevas[b], Jiali Shen[a], Joni Kalliokoski[c], Chao Yan[a], Siddharth Iyer[c], Tuuli Lehmusjärvi[a], Sehyun Jang[a,d], Roseline C. Thakur[a], Lisa Beck[a], Deniz Kemppainen[a], Miska Olin[c], Nina Sarnela[a], Jyri Mikkilä[a,e], Jani Hakala[a,e], Marjan Marbouti[a], Lei Yao[a], Haiyan Li[a], Wei Huang[a], Yonghong Wang[a], Daniela Wimmer[a], Qiaozhi Zha[a], Juhani Virkanen[f], T. Gerard Spain[g], Simon O'Doherty[h], Tuija Jokinen[a], Federico Bianchi[a], Tuukka Petäjä[a], Douglas R. Worsnop[a,i], Roy L. Mauldin III[a], Jurgita Ovadnevaite[g], Darius Ceburnis[g], Norbert M. Maier[j], Markku Kulmala[a,k,l], Colin O'Dowd[g], Miikka Dal Maso[c], Alfonso Saiz-Lopez[b]* and Mikko Sipilä[a]*

[a]Institute for Atmospheric and Earth System Research/Physics, Faculty of Science, 00014 University of Helsinki, Helsinki, Finland.
[b]Department of Atmospheric Chemistry and Climate, Institute of Physical Chemistry Rocasolano, CSIC, Madrid 28006, Spain.
[c]Aerosol Physics Laboratory, Physics Unit, Tampere University, FI-33014 Tampere, Finland.
[d]Division of Environmental Science and Engineering, Pohang University of Science and Technology, Pohang, 37673, Korea.
[e]Karsa Ltd., A. I. Virtasen aukio 1, 00560 Helsinki, Finland.
[f]Department of Geosciences and Geography, University of Helsinki, 00560 Helsinki, Finland.
[g]School of Physics, Ryan Institute's Centre for Climate & Air Pollution Studies, and Marine Renewable Energy Ireland, National University of Ireland Galway, H91 CF50 Galway, Ireland.
[h]School of Chemistry, University of Bristol, BS8 1TS Bristol, UK.
[i]Aerodyne research Inc., Billerica, MA 01821, USA.
[j]Department of Chemistry, Faculty of Science, 00014 University of Helsinki, Helsinki, Finland.
[k]Aerosol and Haze Laboratory, Beijing Advanced Innovation Center for Soft Matter Science and Engineering, Beijing University of Chemical Technology, 100089 Beijing, China.
[l]Joint International Research Laboratory of Atmospheric and Earth System Sciences, Nanjing University, 210023 Nanjing, China.

* Alfonso Saiz-Lopez and Mikko Sipilä
Email: a.saiz@csic.es and mikko.sipila@helsinki.fi

**This PDF file includes:**

Supplementary text S1-S7
Figures S1 to S20
Tables S1 to S7
SI References

## Supplementary Information Text

### S1. Sampling site

An intensive field study was conducted at the Mace Head Atmospheric Research Station, Ireland during the summer period from June 19, to July 19, 2018. The observatory is located on the remote western coast of Galway, Ireland (53°19' N, 9°54' W). This site has a unique marine environment setting characterized by the presence of iodine emitting macroalgae beds, including kelps and other brown algae and parallelly it experiences strong tidal changes. The site is surrounded by small villages, such as Carna and Roundstone, and the nearest city, Galway, is located about 60 km away from the monitoring station on the eastern side, making it a remote site with minimum direct human influence. Occasional biomass burning events were observed in the surrounding areas during the measurement period. Figure S12 shows the location of Mace Head monitoring station. Full description of the site can also be found in other studies (*e.g.* (1, 2)).

### S2. Measurements of gas-phase halogen species

### S2.1. Instrument setup

We deployed a bromide ion based chemical ionization atmospheric pressure interface time-of-flight mass spectrometer (Br-CI-APi-TOF) to Mace Head to measure gas-phase halogenated species. The CI-APi-TOF is similar to the ones deployed in previous works (3, 4), except the mass analyzer unit of the instrument. In this study, a long-TOF has been used, which has a higher mass resolving power of ∼10000 compared to a normal CI-APi-TOF instrument which has a typical mass resolving power of ∼5000 (5). The chemical ionization was achieved using bromide ions instead of nitrate ions, aiming at detecting iodine species such as $I_2$, HOI, ICl, and IBr. This bromide-based chemical ionization technique has been successfully utilized previously for the detection of ambient chlorine species and $HO_2$ radical (6, 7), and has been demonstrated in laboratory conditions to be also capable of detecting iodine oxides, sulfuric acid, and organics (8, 9).

A newly developed multi-scheme chemical ionization inlet (Karsa Ltd.) was deployed in our CI-APi-TOF. The details of the inlet design, setup, and operation of the inlet can be found in Rissanen et al. (9). Briefly, the inlet consists of an electrically grounded 24 mm inner diameter (ID) stainless steel flow tube, coupled with an ion-source. The reagent ion, bromide ($Br^-$), was generated by feeding 25 standard milliliters per minute (mlpm) of nitrogen ($N_2$) flow through a saturator containing dibromomethane ($CH_2Br_2$; >99.0%, Tokyo Chemical Industry) into the ion-source, where the reagent was ionized by soft x-ray radiation (Hamamatsu). The bromide ions were accelerated and focused by different electric fields into the laminar sampling flow of the inlet, through a 5 mm orifice. A small counter-flow (~40 mlpm) was applied through the orifice to prevent the mixing of the electrically neutral ion precursor reagent with the sampling flow.

The sampling flow inlet was set up at approximately 1.6 m above the ground level with a total inlet length of ~1.3 m protruding out through the window of the station. The distance between the bromide ion source and the pinhole (diameter = 0.3 mm) entering the instrument (APi-TOF) was fixed to allow a consistent reaction time. With the total sampling flow rate of being 20 liters per minute (lpm), the total residence time in the sampling line was estimated to be less than 2 s and the reaction time for the bromide reagent ion with sample air was ~30 ms, prior to entering the low-pressure regime of the APi-TOF via the pinhole. The sampling inlet was designed to be essentially a laminar flow through a circular stainless steel tube with an inner diameter of 24 mm and with a fix total flow rate of 20 lpm, the calculated Reynolds' number was about 1000 (refer to Rissanen *et al.* (9) for details of the gas flows and ion paths within the inlet).

During this campaign, the inlet was operated only in bromide ionization mode at the beginning of the measurement (June 18) until June 22, 2018. Starting from the afternoon of June 22, we changed the measurement setup to switch automatically between the bromide chemical ionization (in which we utilized bromide anion to charge neutral molecules) and ambient ion mode (in which the chemical ionization module was disabled to measure ambient charged clusters). Each mode lasted for 10 min and this switching continued until the end of the study (July 19). The data of Br-CI-APi-TOF were collected at 2 s time resolution.

## S2.2. Detection of $I_2$, HOI, ICl and IBr by Br-CI-APi-TOF

The HOI, ICl, IBr, and $I_2$ in the sample air were ionized by $Br^-$, and then detected as clusters of $Br(HOI)^-$, $Br(ICl)^-$, $Br(IBr)^-$, and $Br(I_2)^-$, respectively. Figure S13 shows the example peaks of the charged clusters detected by the Br-CI-APi-TOF during the ambient samplings, along with their peaks detected during background measurements. Well-defined bromide ion-cluster peaks characterized the mass spectrum. For example, it can be seen in the inset of Figure S3B that the three major bromide ion-cluster peaks of $(^{81}Br_3)^-$ at the mass of 242.7494 *m/z* and the $^{79}Br(I^{37}Cl)^-$ and $^{81}Br(I^{35}Cl)^-$ peaks at 242.7893 *m/z* and 242.7902 *m/z* can be easily separated given the high mass-resolution of the instrument. The detected bromide ion-cluster peaks showed a clear negative mass defect with respect to their theoretical values. The overall ambient signals of bromide ion-clusters also showed good agreement of isotopic ratio with their theoretical values (Fig. S14). For example, Fig S14B shows a ratio of $^{79}Br(I^{35}Cl)^-$ and $^{81}Br(I^{37}Cl)^-$ of about 3:1, which is consistent with the pattern expected from the natural isotopic abundances of these elements. We conducted the background measurements both during the field measurements (for 4 different time periods), as well as in the laboratory experiments (post-campaign) using the same setup. The in-field background was determined by flooding the inlet with an excess of nitrogen flow (99.999% of purity) for at least 10 min during the daytime low tide event. The results showed the absence of the species of interest (HOI, ICl, IBr, and $I_2$) when compared to the ambient spectra (see Fig. S13), and there is no significant difference among the background measurements, indicating the background levels of the species of interest are similar over the measurement period.

The inlet wall chemistry/conversion has been a concern in many previous halogen studies. To minimize this effect, our sampling inlet was designed to operate in essentially a laminar flow (see section S2.1) and under laminar flow conditions, only the gas-flow in the middle of the tube is ionized, then enter the low-pressure regime of the instrument via the pinhole, while the rest is exhausted (9). With the known diffusion coefficient of a molecule, we calculated the diffusion time needed for a halogen molecule to reach the inlet wall for wall surface-reaction, or the produced halogen molecule to diffuse from the wall surface to the center-axis of the sampling tube, which will be detected by our instrument. The calculation suggests minimum effect from the wall chemistry since the time needed for a specific halogen species to diffuse along 1.2 cm (radius of the circular sampling tube) is longer (> 4 s as listed in Table S2) than the estimated residence time of the sampling inlet, 1.8 s.

The raw APi-TOF data was processed by using Tofware (version 3.2.0). Before processing, the raw data was pre-averaged over 20 s. Mass calibration was performed using known masses that were persistently present in the spectrum, for instance, the bromide ion ($Br^-$), bromide-water cluster ion ($Br(H_2O)^-$) and tribromide ion ($Br_3^-$). The peak assignment of halogen-containing species including all their isotopes in the mass spectra was performed within a mass tolerance of about 0.1 ppm, and the fitted area ranged from 99 to 101%. The blank signals were subtracted from the preprocessed signal. To take the variation in total reagent ions between laboratory calibrations and during field measurements into account, the ambient concentrations of the detected halogen species were calculated according to the equation given in Eq.S1.

$$[X] = C_X \cdot \left( \frac{^{79}Br(x)^- + {}^{81}Br(x)^- + \ldots}{^{79}Br^- + {}^{81}Br^- + {}^{79}Br(H_2O)^- + {}^{81}Br(H_2O)^-} \right) \qquad \text{(Eq.S1)}$$

Where, *C* is the calibration coefficient and X represents $I_2$, HOI, IBr or ICl, respectively. To minimize the error in accounting for the variability of reagent ions during field measurements, the sum of ambient signals of halogen species, including their isotopes, were normalized with the sum of bromide ions and bromide water cluster signals. The inclusion of $Br(H_2O)^-$ cluster into Eq.S1 also aims to minimize the effect of ambient water humidity in our results (10). The final ambient concentrations were then averaged to 1-minute intervals for further analysis. In this study, we focus only on the measurements with bromide ion chemical ionization therefore the measurements in the atmospheric negative ion mode were removed. With the background information and the calibrations (to be presented in the following sections), the limits of detection (LOD) were determined to be 0.09, 0.15, 0.08, and 0.07 pptv (1 min-average, 3$\sigma$) for HOI, ICl, IBr, and $I_2$, respectively.

### S2.3. Calibration of $I_2$

We conducted post-campaign calibrations of the instrument for $I_2$, HOI, and $Cl_2$ with the same field inlet setup and instrument settings used during the field measurement in our laboratory of the University of Helsinki.

For the iodine calibration, different known concentrations of $I_2$ were introduced via the inlet of the Br-CI-APi-TOF using a nitrogen carrier stream at 23 lpm. The iodine sample streams were produced by passing 50 mlpm of pure $N_2$ through a heating device holding an iodine permeation tube (VICI Metronic). The heating device (for holding the permeation tube) was made from a stainless steel tube (½-inch outer diameter, OD) with a length of 25 cm, encased within an electronically controlled heating mantle. The latter allowed reliable temperature adjustment in the range of 80 to 140 (± 2) °C, and thus convenient variation of the relative iodine concentrations in the carrier gas stream. Prior to calibration experiments, the $I_2$ source was run continuously for at least 72 hours to ensure complete system equilibrium. After that, we conducted testing by continuously injecting the $I_2$ sample streams into the Br-CI-APi-TOF for over 24 hours, and the signal intensities remained constant, suggesting that the output of the $I_2$ source was sufficiently stable to allow reliable calibration experiments.

The $I_2$ concentration permeated from the permeation device heated at 140°C was determined by two different analytical methods. Firstly, we follow the method of Chance et al. (11) involving the absorption of iodine in n-hexane at cryogenic temperatures, followed by quantification by Vis-spectrophotometry. The iodine trapping experiments were carried out in an all-glass apparatus, mounted in a well-vented hood. The absorption vessel was filled with 20 ml of n-hexane (99.95%, Merck), and then weighed to determine the combined mass. The loaded absorption vessel was fitted with a glass inlet tube, which was secured with a steel clamp, and subsequently connected to the corresponding Teflon inlet and outlet gas lines. The fully assembled absorption unit was immersed into a wide-necked Dewar vessel filled with an acetone/dry ice mixture (−80±3°C) to such a depth as to match the n-hexane level with that of the cooling medium. After temperature equilibration, the gas stream emerging from the permeation oven (nitrogen flow rate of 50 mlpm, oven temperature of 140°C) was allowed to pass through the absorption unit for 5 hours. After this experimental step, it was observed that a small purple deposit had formed at the immersed tip of the inlet capillary, most probably consisting of frozen water supporting adsorbed iodine. Therefore, after stopping the carrier gas stream, the absorption apparatus was removed from the cooling mixture, and allowed to warm to room temperature prior to disassembling the setup to prevent any losses of iodine. The absorption vessel containing the hexane solution was re-weighed and its mass was compared with that obtained prior to absorption. The difference in mass was observed to be less than 2%, indicating that the loss of n-hexane was rather negligible. The sample solutions were stored in the refrigerator (4°C) for 14 hours before being subjected to analysis. The iodine content of the samples was determined using an UV/Vis spectrophotometer (Shimadzu Model UV2450) at a wavelength of 522 nm using 5 cm-length glass cuvettes. Calibration curves were generated from standard solutions ranging from 270-5300 nmol of iodine, by dilution of a freshly prepared stock solution (50 mg of iodine in 100 ml of n-hexane) with n-hexane. To avoid potential carry-over effects, the cuvettes were rinsed thoroughly with the solvent in between measurements. Sample solutions analyzed after being stored at 4°C in glass containers sealed with Teflon coated glass stoppers for 2 days and 7 days produced essentially identical results, thus providing evidence that the iodine concentrations remain essentially uncompromised under these storage conditions. Following an alternative analytical approach, we also quantified iodine in the absorption solution using an inductively coupled plasma mass spectrometry (ICP-MS) based method. For this purpose, the hexane solutions were treated with aqueous 0.100 M $NaHSO_3$, accomplishing efficient hexane-to-water extraction and simultaneous reduction of iodine to iodide (12), followed by quantification using an Agilent 7800 ICP-MS (Agilent Clinical Sample Preparation Guide (v3), *ref.* ISO 17294-2). The results obtained were in good agreement with those obtained by the UV/Vis spectrophotometric method outlined above. The iodine trapping and quantification experiments were carried out in triplicate with satisfactory reproducibility, with the emerging results allowing the calculation of an iodine permeation rate of 278 ± 12 ng min$^{-1}$ (mean ± standard deviation). This result was used as the benchmark for estimating temperature-corrected permeation rates according to the formula provided by the permeation tube vendor (VICI Metronic). The validity of the temperature-corrected values was checked by conducting another iodine absorption experiment in which the iodine permeation tube was kept at 130°C, and the determined permeation rate agreed satisfactorily with the calculated value (within 10%).

Figure S15 shows the plot of $I_2$ concentration versus the measured normalized signal of $I_2$. It is noted that the instrument responded linearly to $I_2$ at concentrations below 180 pptv, and 'non-linearly' at high $I_2$ concentration. This was most likely due to the depletion of the reagent bromide ions in the instrument. For this study, we used the calibration coefficient determined from the slope of linear-fitting (2676 pptv with a $R^2$ of 0.98) for the $I_2$ data processing since the majority of the ambient data points (>99.97%) fall within this regime. While the data points that fall out of the linear regime was corrected using the exponential fit function ($f(x) = (245.1\exp(1.309(x))) + (-245.8\exp(-13.44(x)))$). We have also investigated potential changes in the $I_2$ detection sensitivity that may occur due to variation in humidity in the sample stream, and found that this factor does not affect the measurements significantly when normalizing the $I_2$ signal with the sum of $Br^-$ and $Br(H_2O)^-$, as shown in Eq.S1 (10). Therefore, our $I_2$ measurement at Mace Head is not affected by the changes of ambient humidity. The total uncertainty for $I_2$ detection by Br-CI-APi-TOF was calculated to be ± 45%.

## S2.4. Calibration of HOI

The main challenge is that there is no HOI standard available commercially which can produce an appropriate amount of HOI concentration for mass spectrometry calibration. We developed a continuous HOI source in our laboratory by reacting $I_2$ with hydroxyl radical (OH) using a similar setup as used for the sulfuric acid ($H_2SO_4$) calibration (9, 13). The OH was generated by the photolysis of $H_2O$ with a mercury (Hg) lamp at 184.9 nm and the OH concentration was calculated with the calibrated lamp intensity flux, which was determined by the conversion of $N_2O$ to $NO_x$. The procedures of OH concentration calculation and $N_2O$ actinometry experiment are described in detail in Kürten *et al.* (13). For this calibration, a known amount of $I_2$ was mixed with 23 lpm of $N_2$ flow before passing through the calibrator. Then the outgoing airflow was sampled by the Br-CI-APi-TOF keeping the inlet-length and sampling flow rate similar to that of the field setup. We tested the system by removing the $I_2$ or OH source from the calibrator, upon which HOI production was undetectable, confirming that the production of HOI in this system requires both $I_2$ and OH.

A numerical model was constructed based on the model that was specific for $H_2SO_4$ calibration (refer to Kürten *et al.*, (13) for details) to calculate the mean HOI concentration at the end of the sampling inlet, prior to being ionized by the bromide reagent ion. This was done by substituting the relevant chemical reactions and input parameters with iodine chemistry related reactions and input parameters. Figure S16A shows the reaction scheme used for modeling the HOI concentration in the calibration system. The input parameters used in the model were the inner tube diameter, the length of the tube, the total flow rate of the inlet, the lamp intensity flux derived from the $N_2O$ experiment, the gas temperature (T) as well as the concentrations of $I_2$, $O_2$, and $H_2O$. This model only considered the reaction of $I_2$+OH to produce HOI (R.S1), while other HOI production pathways, like IO+$HO_2$ (R.S3), were considered unimportant in this calibration system. This assumption is justified because we expect the presence of a very low level of IO, given the likely negligible $O_3$ concentration in the system and the slow reaction rate of I+$O_3$ (see R.S2). Another potential source of IO is via the loss of HOI with OH (R.S4) in the system (14), but this reaction has a rate of about two orders of magnitude slower than the reaction of $I_2$+OH (R.S1). Thus, it likely cannot provide sufficient IO for R.S3 to occur within the short inlet residence time (< 2 s) and thus HOI loss of via the R.S4 pathway will not significantly affect the final concentration of HOI in the calibration system.

$$I_2 + OH \overset{k_{S1}}{\rightarrow} HOI + I \qquad (k_{S1} = 2.1\times10^{-10}\ \text{molecule cm}^{-3}\ \text{s}^{-1}\ \text{at 298 K}) \qquad \text{R.S1}$$

$O_3 + I \xrightarrow{k_{S2}} IO + O_2$ ($k_{S2} = 1.3\times10^{-12}$ molecule cm$^{-3}$ s$^{-1}$ at 298 K) R.S2

$HO_2 + IO \xrightarrow{k_{S3}} HOI + O_2$ ($k_{S3} = 8.4\times10^{-11}$ molecule cm$^{-3}$ s$^{-1}$ at 298 K) R.S3

$HOI + OH \xrightarrow{k_{S4}} IO + H_2O$ ($k_{S4} = 5.0\times10^{-12}$ molecule cm$^{-3}$ s$^{-1}$) (14) R.S4

For species of $I_2$, OH, and HOI, wall loss was taken into account. The diffusion coefficients used in the model calculation were adopted from previous studies (15-17). The reaction rate coefficients (*k*) were obtained from the IUPAC kinetic database (18) unless cited.

Figure S16B displays the normalized signal of HOI corresponding to different HOI concentrations generated from the reaction R.S1 by both varying the amount of OH and $I_2$ concentrations in the calibrator. A linear correlation between the modeled HOI concentrations and measured signals is observed ($R^2 = 0.97$), yielding a slope of 12199 pptv. This excellent correlation also indicates that the changes of the humidity (from the variation of $H_2O$ for production of OH) in the calibration system may not affect the sensitivity of the HOI detection by Br-CI-APi-TOF, hence, ambient humidity should have little influence on our HOI measurement. Upon checking the ambient data, we found no clear relationship between the overall measured HOI and ambient humidity ($R^2 = 0.02$). In view of the assumptions and uncertainties from the calibration and HOI model calculation, the reported value of HOI in this study was considered as a lower limit with an estimated total uncertainty of ± 55%.

### S2.5. Estimating the calibration coefficient for ICl and IBr

Although analytical calibrations were carried out in this study for $I_2$ and HOI, performing the calibrations for ICl and IBr was still challenging, especially in the context of producing and quantifying a stable low-concentration ICl or IBr primary standard. Therefore, we combined the information from the quantum chemical calculation and the calibration experiments of $I_2$, HOI, $Cl_2$ and $H_2SO_4$ to obtain calibration coefficients for the detection of ICl and IBr in this study. We calculate the cluster formation enthalpies for $(ICl)Br^-$, $(IBr)Br^-$, $(I_2)Br^-$, $(Cl_2)Br^-$ and $(H_2SO_4)Br^-$ anions, in order to gain information on the binding strength of the charged clusters.

Table S3 shows the cluster formation enthalpies of five major bromide anion clusters corresponding to their determined calibration coefficients. While collision induced cluster fragmentation is an important source of error to weakly-bonded charged clusters (19), it has almost no effect on strongly-bonded charged clusters, which in turn, can be detected at the kinetic limit. For example, Lopez-Hilfiker *et al.* (20) showed that malonic acid has a low cluster formation enthalpy of −27.8 kcal mol$^{-1}$ with iodide anion ($I^-$), and concluded that malonic acid was detected at collision-limited sensitivity. It can be seen that the calculated cluster formation enthalpy of $I_2$ with $Br^-$ was −33.7 kcal mol$^{-1}$, which is slightly more negative than the value of malonic acid iodide cluster. A comparison of the calibration coefficients of $I_2$ with $H_2SO_4$ in our instrument showed a difference of less than a factor of 2 which was in the range of uncertainties of $I_2$ and $H_2SO_4$ detections. Since the clustering energy of $H_2SO_4$ with bromide was also very low (−41.1 kcal mol$^{-1}$), and the detection of $H_2SO_4$ by nitrate and bromide chemical ionization methods are expected to be efficient (21, 22), both $I_2$ and $H_2SO_4$ were very likely detected at the kinetic limit. On the other hand, the detections of $Cl_2$ and HOI showed to have much lower sensitivities than the $I_2$ and $H_2SO_4$ as their clusters with bromide anions are considerably less stable compared to $(I_2)Br^-$ and $(H_2SO_4)Br^-$. With the fact that the ICl and IBr could form more stable charged clusters with $Br^-$ (−33.8 kcal mol$^{-1}$, −36.7 kcal mol$^{-1}$, respectively) as compared to $(I_2)Br^-$ and malonic acid-iodide clusters, it strongly suggests that ICl and IBr are detected in the kinetic limit regime, and hence likely have sensitivities similar to $I_2$ or $H_2SO_4$.

To be more conservative, we applied the calibration coefficient of $H_2SO_4$ to ICl and IBr in this study to give a lower limit of the ICl and IBr ambient concentration. It should be noted that the changes of ICl and IBr sensitivity within the calibration coefficients of $I_2$ and $H_2SO_4$ do not affect the overall conclusions of this study. Further calculations showed that other pathway of formation and loss of ICl and IBr with $Br^-$ were unimportant, as they required much higher energy barriers for the reactions to proceed (see Table S3). Given the similarities shared between ICl or IBr and $I_2$, we expect that the ambient humidity should also have a minor effect on the detection of ICl and IBr, as mentioned in the $I_2$ calibration experiments (see section S2.3). We predicted the total uncertainty of our ICl and IBr measurements to be within a factor of two (± 200% + LOD), mainly propagated from the combined error of the quantum chemical calculation and the measurements uncertainties of $I_2$ and $H_2SO_4$ species. Note that the inclusion of LOD into this uncertainty is to account for the increasing error near the LOD of the measurements. The following sections describe the detailed procedures for the quantum chemical calculation, calibration of $Cl_2$, inter-calibration of $H_2SO_4$, and IBr peaks identification.

**Quantum chemical calculation.** The initial conformer sampling was performed using the Merck Molecular Force Field with the Spartan '18 program (23-26). These conformers were then optimized using Density Functional Theory (DFT) methods at the ωB97X-D//aug-cc-pVTZ-PP level. Iodine and bromine pseudopotential definitions were taken from the EMSL basis set library (27). Calculations were carried out using the Gaussian 09 program (28). Additionally, a coupled-cluster single-point energy correction was carried out on the lowest energy ωB97X-D//aug-cc-pVTZ-PP geometries. DLPNO-CCSD(T)/def2-QZVPP level theory was carried out in ORCA program ver.4.1.1 (29, 30). The accuracy of the method has been previously tested by comparing the DLPNO-CCSD(T) calculated formation enthalpies for a set of 113 molecules with their accurate formation enthalpies and found to have a mean absolute error of 1.6 kcal $mol^{-1}$ (31). Formation enthalpies were calculated by H(product) – H(reactants), where H denotes quantum chemically calculated enthalpies.

**Calibration of $Cl_2$.** Although we did not observe $Cl_2$ signal at Mace Head, we performed a $Cl_2$ calibration in the laboratory to check on the sensitivity of the instrument towards $Cl_2$.The determination of the amount of chlorine liberated from a commercial chlorine permeation tube (VICI Metronic) was carried out following a procedure described previously (32). For this purpose, a 20 mlpm of high purity nitrogen (99.999%) was passed through a stainless steel sample holder (½-inch O.D. tubing with a length of 25 cm), containing the chlorine permeation tube, at room temperature. The output flow was bubbled into a buffered aqueous potassium iodide solution (2.00% KI, (*m/v*) prepared in 1.00 mM aqueous phosphate buffer, pH = 7.0) contained in an all-glass two-stage serial absorption apparatus (stage 1 = 100 ml; stage 2 = 50 ml) for 3 hours and kept at room temperature (24°C). Upon contacting the KI absorption solution, chlorine oxidized the iodide into iodine, which then further reacted with the excess KI present in the absorption solution to form $I_3^-$, an analytical species that can be readily quantified by UV/Vis-spectrophotometry. The employed serial two-stage absorption configuration allowed the evaluation of the chlorine trapping efficiency by analyzing the respective solutions separately. Gratifyingly, none of the analytical $I_3^-$ species could be detected in the second stage absorption solution, indicating that all the chlorine was quantitatively trapped and rapidly converted to $I_3^-$ within the first absorption unit. The emerging sample solutions were analyzed with an UV/Vis spectrophotometer (Shimadzu Model UV-1800) using 1.00 cm quartz cells at 352 nm. The samples were quantified relative to $I_3^-$ standards (5 to 68 x $10^{-6}$ mol $L^{-1}$) prepared by dilution of a stock obtained by dissolving 174 mg iodine in 200 ml of a solution containing 2.00 % KI in 1.00 mM aqueous phosphate buffer, pH 7.0. From the calibration curve obtained with these standard solutions for $I_3^-$ at 352 nm (Fig. S17A), a molar absorptivity of 26,800 L $mol^{-1}cm^{-1}$ was calculated, which is consistent with the values reported in the literature (32, 33). Samples and standard solutions were re-analyzed after being stored in the dark at 23°C for 24 hours, and the results did not differ significantly (less than 3%) from those obtained with the fresh solutions. The average chlorine permeation rate calculated from the results of two room temperature (at 24°C) absorption experiments was 764 ± 74 ng $Cl_2$ $min^{-1}$ (mean ± standard deviation).

Prior to calibration experiments, the $Cl_2$ source was run continuously for 12 hours to ensure complete system equilibrium. To obtain lower concentrations of $Cl_2$ (in pptv level), the output of the permeation was diluted by a two-stage dilution system similar to the setup of Gallagher *et al.* (34). A 20 mlpm of $N_2$ stream emerging from the $Cl_2$ permeation device (operated at room temperature) was diluted in a stream of 6 lpm of dry $N_2$. Only a small fraction of this mixture (50 – 300 mlpm) was further diluted by the total flow of 25 lpm of $N_2$ (20 lpm dry $N_2$ + 5 lpm humidified $N_2$) before being sampled by the Br-CI-APi-TOF. The overall calibration coefficient for $Cl_2$ was determined to be 14599 pptv from three separate experiments (Fig. S17B), with an accuracy of 30%. The calculated LOD for $Cl_2$ is 1.1 pptv (1 min-average, 3σ).

**Inter-calibration of $H_2SO_4$.** In this study, a concurrent measurement of sulfuric acid ($H_2SO_4$) by a nitrate chemical ionization mass spectrometer (nitrate-CIMS) (35) was carried out. The calibration factor of $H_2SO_4$ ($3.8 \times 10^9$ molecule $cm^{-3}$) of the nitrate-CIMS was obtained from the relative calibration of $H_2SO_4$. The detailed description of the calibration system was given in previous studies (36, 37). To summarize, the calibration was performed by producing a known amount of OH in front of the sampling port. Light passes from a temperature-controlled Hg lamp and was then reflected off by two mirrors mounted at 45° to the light path. These mirrors were coated to selectively reflect the wavelenghth of 184.9 nm. Light exits the calibration housing through a Suprasil window before illuminating the sample flow. The calibration housing was $N_2$ purged to prevent light absorption and the build up of $O_3$ from the photolysis of $O_2$. The OH concentration produced by the calibration source is a function of the intensity of the photon flux at 184.9 nm, the concentration of water vapor ($[H_2O]$), the absorption cross-section at 184.9 nm, the yield of OH from $H_2O$ photolysis, and the sample flow velocity. The flow velocity was measured using a hot wire anemometer, and the $[H_2O]$ was measured using a dew point hygrometer. The photon flux at 184.9 nm was mapped out using a vacuum UV diode mounted on an x/y movable traverse. This vacuum UV diode was intercompared with a National Institute of Standards and Technology (NIST) standard diode to determine the quantum efficiency. For this work, the value of $7.14\text{x}10^{-20}$ $cm^2$ $molecule^{-1}$ from Cantrell *et al.* (38) was used for the $H_2O$ absorption cross-section as it is in good agreement with other measurements, and this value has been used for the reported values in earlier work (35, 39). The determined $H_2SO_4$ from nitrate-CIMS was used to inter-calibrate the $H_2SO_4$ detected by our Br-CI-APi-TOF. Figure S18 shows the plot of $H_2SO_4$ measured by nitrate-CIMS *vs.* the signal of $H_2SO_4$ and the slope of 1418 pptv ($R^2$ =0.91). The total uncertainty was ± 45% referring to the total systematic and random errors for a given measurement.

**IBr peaks identification**. In addition to the calibrations of different species, we also conducted a qualitative testing in the laboratory to confirm that the detected peaks in the ambient air correspond to the iodine interhalogen species. We spiked a 10 µL of an unknown concentration of IBr mixed in $N_2$ into the main stream of the sampling inlet (with 25 slpm of $N_2$ flow; RH of the flow = ~25%; at room temperature). The 10 µL of IBr-laden $N_2$ gas was taken with a gas-tight syringe (100 µL, 1700 series, Hamilton) from the headspace of solid IBr (99.8%, Sigma-Aldrich), which was held in a glass flask and purged with a 50 mlpm of dry $N_2$. The solid IBr was handled in an oxygen-free fume hood, and kept in dry $N_2$ prior to usage, to prevent chemical reactions of IBr involving $O_2$ and humidity. From four repetitions of the spiking tests, our instrument shows almost instantaneous responses (sharp increase and decrease; Fig. S19), and confirm that the measured ambient peak at 284.7414 m/z corresponds to the $^{79}Br(I^{79}Br)^-$ peak from the standard (matching with all of its isotopes as well), as shown in the inset of Figure S19. We did not observe any increment of the fragment of halogen ions related to IBr during the test.

## S3. Ancillary Measurements

Table S4 summarizes the list of key instruments used in this study. Other supporting measurements included the gas-phase, aerosol-phase and meteorological parameters. Apart from the halogen species measurements, the Br-APi-TOF was also used to detect the $HNO_3$ signal (associated to $NO_3^-$ at 61.9884 *m/z*, not calibrated) during this study. The $O_3$ and carbon monoxide (CO) were measured by an $O_3$ analyzer (Thermo, 49i) and a CO analyzer (Trace Analytical RGA3), respectively. The instruments employed for aerosol measurements include: particulate matter of 2.5 and 10micron, $PM_{2.5}$ and $PM_{10}$ (TEOM model 1405), an SMPS (20-500, Vienna type DMA, TSI 3010 CPC). An aerosol mass spectrometer (Aerodyne HR-ToF-AMS) was used to measure the size resolved non-refractory chemical composition of submicron aerosol particles (*i.e.* iodide and sulfate) and the mass concentration of submicron particulate matter ($PM_1$) (40). The HR-ToF AMS was routinely calibrated according to the methods described by Jimenez et al. (2003). Measurements were performed with a time resolution of 5 min, with a vaporizer temperature of about 600ºC. Iodide in HR-ToF-AMS is represented by a signal at 126.9044 *m/z*, which is a non-refractory $I^-$ ion, but due to fragmentation in the instrument, molecular information on $I^-$ is not available. The LODs for standard HR-ToF AMS species are reported in DeCarlo *et al.* (40) and are equal to 22, 5.2, 2.9, 38, and 12 ng $m^{-3}$ for organic matter (OM), sulfate, nitrate, ammonium and chloride, respectively. The LOD for $I^-$ was calculated following the procedure in DeCarlo *et al.* (40) and is equal to 0.3 ng $m^{-3}$.The data from respective meteorological sensors were used in this study for parameters like relative humidity (RH), temperature, wind profile, and solar radiation. The tide heights and time were recorded from Roundstone Bay which is located at the opposite shore, north of the Mace Head station (see Fig S12), and the data was procured every day from the website of Tide Times (https://www.tidetimes.org.uk/).

## S4. Calculation of aerosol-surface area

To estimate the surface area of aerosols for each measurement, we used information from the size distribution measurements and the particulate matter mass measurements. Detailed size distributions were available for particles in the size range below 1 μm. Additionally, the mass of $PM_{2.5}$ and mass in the range from 2.5 to 10 μm ($PM_{2.5-10}$) were also available during the measurements.

Using these data, an estimation of the particle mass distribution was made based on information from an earlier publication on typical aerosol mass distributions at the Mace Head. According to Yoon *et al.* (41), the typical supermicron mass distribution has two log-normal modes with peaks at approximately 2.0 μm and 8.0 μm. Using this information together with measured size distribution information, we employed least-square optimization to estimate the particle mass distribution that reproduced the observations.

Once the mass distribution was estimated, it was converted to number distributions to compute particle surface areas. To this end, the observations were corrected for humidity since the measured particle sizes were obtained from a dried aerosol, while the actual surface area relevant to our study was in ambient humidity. Separate corrections were applied for the sub-micron SMPS observations and the estimated supermicron data. For the submicron data, a hygroscopicity parameterization developed by Laakso *et al.* (42) was used to convert particle sizes from dry to ambient humidity state. For the supermicron particles, the wet particle size was estimated using the kappa parameterization (Eq.S2).

$$\text{G.F.} = \left(1 + \text{kappa} \times \left(\frac{RH_i}{100 - RH}\right)\right)^{1/3} \qquad \text{(Eq.S2)}$$

The kappa value used was 1.2 based on the value given in Nguyen et al. (43) for pure NaCl. However, it could be likely an overestimation; *e.g.*, Zieger *et al.* (44) proposed a kappa value of 1.1 for inorganic sea salt particles.

The largest uncertainties in the calculation of the total aerosol surface area are related to the estimation of supermicron aerosol number and size (from the mass concentration measurements by dual channel TEOM in fine and coarse size fractions simultaneously) and the effect of hygroscopic growth (due to the unknown hygroscopicity parameter). The surface area computed from submicron (SMPS) dry size distribution can with high confidence be considered as the absolute minimum possible surface area. To obtain the supermicron particle number and size, several assumptions were made: the supermicron mass distribution was estimated to be consisting of two log-normal modes with geometric means of 2.0 and 8.0 μm (41). Due to measurement gaps in fine or coarse size fraction mass (1.0-2.5 μm or 2.5-10 μm) by TEOM run at 6 min time resolution, the best estimate-based gap filling was attempted by using observed correlations between SMPS observations and supermicron mass as a proxy. As the correlation between SMPS and supermicron mass was low for masses < 2 μg $m^{-3}$, such values were gap-filled using a running median from temporally close data.

The sensitivity of the computed surface area to the assumed mass median diameters of the supermicron mode could not be directly estimated due to the fitting procedure used in deriving the size distribution. To predict the uncertainty caused by the estimated size of these modes, we performed series of runs of the fitting procedure for the measured data points by varying the mode sizes and analyzing the obtained surface area values. Those mode sizes were randomly selected from a normal distribution centered at the original value and with $\sigma$ = 0.4 and 1.6 for the two supermicron range peaks, respectively. Varying the mode sizes resulted in aerosol surface area with no clear dependence on the input values (Fig. S20A, upper panels). The low number concentration and the fact that the fitting is constrained by the mass observation are the reasons behind the low sensitivity. For these reasons, we are confident that there is insignificant systematic dependence on the choice of diameters for supermicron particle size distribution fitting.

The same procedure was applied for estimating sensitivity of the selected $\kappa$ value. The value of the hygroscopicity parameter was expected to have an influence on the computed surface area, as hygroscopic growth may increase the particle volume significantly. We saw that a change of 0.1 in $\kappa$ resulted in an approximately 3% change in the computed average surface area (Fig. S20B). From this, we estimated that the effect of the hygroscopicity parameter is mostly *ca.* 10%; and by using $\kappa = 1.2$, the surface area was likely overestimated. The total uncertainty due to mode positions and the kappa values are illustrated in Figure S20A (lower panels): on the left, a histogram of the relative variation caused to each data point with the mode positions and varied kappa values is shown. The mean difference between the obtained maximum and minimum value was 17% of the observed value. On the right panel, an outtake of the data is shown with the shaded area showing the obtained maximum and minimum surface when varying the peak positions and $\kappa$ parameter.

The remaining uncertainty of the surface area concentration is related to the uncertainty of the aerosol number concentration measurement. The main uncertainty in particle size distribution measurements are generally related to charging efficiency, line losses and counting statistics. Uncertainty due to unknown charging efficiency is generally highest for small (< 50 nm) particles, which contribute little to the particle surface area. Line losses have been corrected for. The relative error due to particle counting statistics decreases with longer sampling times: for the 10-minute measurements, the uncertainty of the number concentration measurement is reduced and we expect it to be below 10%.

In total, we estimate that the uncertainty of the surface area estimation is below 30% for most of the observations. Figure S2B shows the time series of the derived aerosol surface area from June 19 to July 19, 2018. The derived range of aerosol surface area in this study is similar to the values reported in the previous study at Mace Head (45).

## S5. Modeling of halogen chemistry

Tropospheric Halogen Chemistry Model (THAMO) (46) is a one-dimension (1-D) chemical transport model and has been used in previous works to study the effect of halogen chemistry in different locations and environments (46-51). THAMO model framework has been documented in detail in Saiz-Lopez *et al.* (46) and is briefly described here. THAMO model contains three parts including a comprehensive chemical scheme (photolysis, gas-phase, and heterogeneous chemical reactions of halogen, oxygen, hydrogen, nitrogen, and sulfur species), a radiation scheme that computes the solar radiation, and a 1-D (vertical) transport module. The chemical mechanism used in the present study is depicted in Table S5.

The THAMO model contains 200 stacked boxes at a vertical resolution of 5 m (total height 1 km) and a time step of 30 s. THAMO was run for 18 consecutive days from June 26 to July 14 in the year of 2018. The main reason for choosing this period for analysis is the full-availability of observed values to be incorporated into the model. All of the observed data were then interpolated into a 30 s interval for the model input. Some species (*e.g.* VOCs, $NO_x$) used in the present study were constrained with representative measured values in the marine boundary layer (47, 48, 52-54) as shown in Table S6, in which the $NO_x$ values were scaled using the variation of normalized

$HNO_3$ signal detected by the Br-CI-APi-TOF. The observed trend of solar radiation was used to scale the photolysis rate of all species. In this analysis, we set the sources of bromine and chlorine species to be zero during the model calculation due to the lack of direct measurements of these species to validate the model performance of bromine and chlorine chemistry. We also ignored the sources of organic iodine species in the analysis since we did not have direct measurements, and previous studies showed that the organic iodine species played a relatively minor role in the total iodine loading compared to $I_2$ at Mace Head (*e.g.* (55, 56)).

To critically evaluate the behavior of iodine species under different conditions, we designed six different scenarios as indicated in Table S7. The measured $I_2$ and HOI were constrained in all model simulations. Simulations 1, 2, and 3 were conducted to explore the potential formation rate of ICl and IBr required to reproduce their observed levels. This was achieved by varying the heterogeneous uptake coefficient of HOI ($\gamma$ = 0.1, 0.3, and 0.9) onto aerosol surfaces with the yield of both ICl and IBr being 0.5. Simulations 2 and 4 were used to explore the effect of $NO_2$ level on the simulation of $IONO_2$ mixing ratio by doubling the amount of $NO_2$. Finally, simulations 5 and 6 were performed to assess the impacts of IBr and ICl on the recycling of atomic I production rate, $HO_x$ production rate, and the iodine-catalyzed $O_3$ loss rate. The output from the first layer of the model was extracted and used for the analysis in this study. The photolysis rates obtained from the model were used to calculate the contribution of photolysis of different iodine species (*i.e.* $I_2$, HOI, ICl, IBr, IO, OIO, and $IONO_2$) to the atomic I production rate.

## S6. Calculation of production rate of ICl and IBr

In order to gain insight into the production pathways of ICl and IBr at Mace Head, the heterogeneous production rate of ICl and IBr was compared with the gas-phase production rate of ICl and IBr:

**Heterogeneous ICl and IBr production rate.** With the steady-state assumption and assuming that HOI heterogeneous uptake is the only source for ICl and IBr production, the production rate of ICl and IBr via reaction of HOI on aerosols can be expressed as in Eq.S3, where A equals to ICl or IBr. The heterogeneous production rate coefficient of ICl and IBr ($k_A$) was calculated by constraining the measured ICl, IBr, and HOI together with the photolysis rates ($j_A$) of ICl and IBr obtained from the THAMO model. Based on this, we estimated that the average heterogeneous production rate of ICl and IBr via HOI during daytime low tides were 0.023 pptv $s^{-1}$ and 0.040 pptv $s^{-1}$, respectively.

$$k_A\,[HOI] = j_A[A] \qquad \text{(Eq.S3)}$$

**Gas-phase ICl and IBr production rate.** ICl and IBr can also be produced via the gas-phase reactions as shown in R.S5 and R.S6, respectively. The reaction coefficients were obtained from the IUPAC kinetic database (18) and have been multiplied by their production branching ratio of 0.2 (for R.S5) and 0.05 (for R.S6).

$$IO + ClO \xrightarrow{k_{S5}} ICl + O_2 \qquad (k_{S5} = 2.4\times10^{-12}\ \text{molecule cm}^{-3}\ \text{s}^{-1}\ \text{at 298 K}) \qquad \text{(R.S5)}$$

$$IO + BrO \xrightarrow{k_{S6}} IBr + O_2 \qquad (k_{S6} = 4.3\times10^{-12}\ \text{molecule cm}^{-3}\ \text{s}^{-1}\ \text{at 298 K}) \qquad \text{(R.S6)}$$

No direct measurement of ClO has been reported at Mace Head (57, 58) but according to a recent halogen-model study, ClO concentration is very low (<< 1 pptv) at the surface-level of marine environment outside of polar region (*e.g.* (59)). Thus, we assumed a large concentration of 1 pptv of ClO as an upper limit for this calculation. We adopted a daytime average of 2.3 pptv for BrO from a previous measurement at Mace Head (60). The mean IO concentration used for the calculation was 5 pptv, a typical value at Mace Head (57). With this information, the production rate of ICl through IO+ClO was calculated to be 0.0003 ppt $s^{-1}$, while the production rate of IBr via IO+BrO was 0.001 ppt $s^{-1}$. (61)

## S7. Calculation of steady-state ICl and IBr

To explore the possibility of the earlier model study in predicting significant levels of daytime ICl and IBr, we performed a simple calculation exercise of steady-state mixing ratio of daytime ICl and

IBr at Mace Head (MH) and Cape Grime (CG), based on the similar criteria as reported in McFiggans *et al.* (61), except different HOI uptake coefficient (γ), using equation Eq.S4.

$$\frac{d(A)}{dt} = \frac{0.5 \times \frac{1}{4} \times C \times S \times \gamma \times [\mathrm{HOI}]}{\text{photolysis rate of } A} \qquad \text{(Eq.S4)}$$

Where $A$ is mixing ratio of ICl or IBr, $C$ is the molecular speed of HOI, $S$ is the aerosol surface area, and [HOI] is the mixing ratio of HOI. The adopted daytime HOI mixing ratios are 11.2 pptv (for MH) and 4.7 pptv (for CG); average aerosol surface area are 60 $\mu m^2$ $cm^{-3}$ (for MH) and 50 $\mu m^2$ $cm^{-3}$ (for CG); the yield of ICl and IBr is 0.5 each; and the photolysis rates of ICl and IBr at these two sites can be found in Table 2 in McFiggans et al. (61). If a higher γ value is used (*e.g.* 0.3 – 0.9) and with an assumption that the HOI mixing ratio remains constant, noticeable levels of ICl and IBr (up to 0.9 pptv) could be accumulated during the daytime at Mace Head and Cape Grim (Fig. S11).

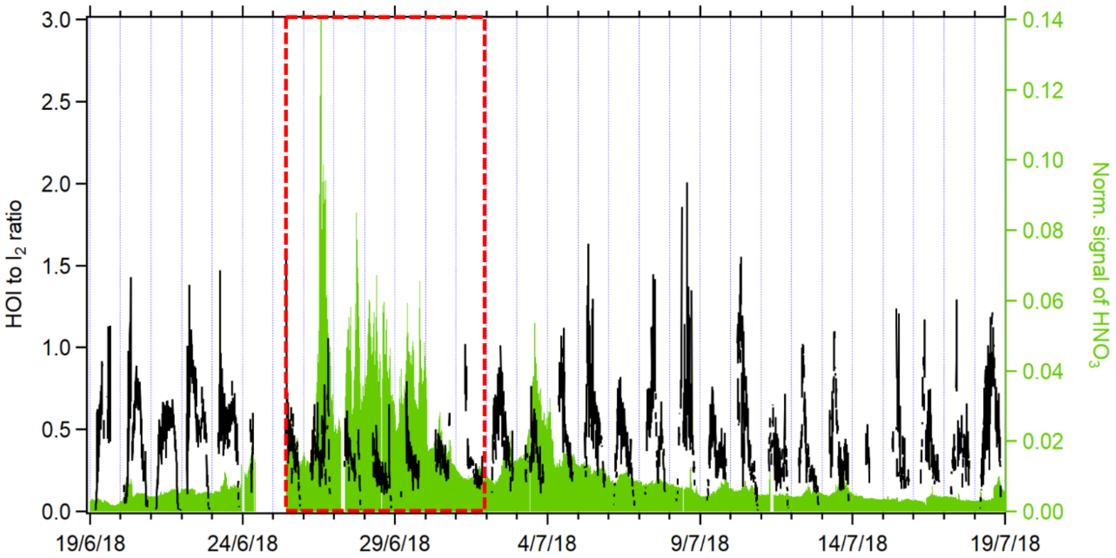

**Figure S1.** The HOI to $I_2$ ratio and the corresponding normalized signal of $HNO_3$ during the campaign. The period with relatively smaller HOI to $I_2$ ratio during the high $O_3$ episode is marked with the red-dashed box. Measurement of nitrogen oxides are not available in the study, therefore, the normalized signal of $HNO_3$ (associated to $NO_3^-$ at 61.9884 *m/z*, not calibrated) is only used to indicate the nitrogen oxides ($NO_x$) trend in the study. It is well known that $HNO_3$ can be originated from the reaction of $NO_x$ with OH and heterogeneous uptake of $N_2O_5$ (formed via reactions of $NO_x$ +$O_3$). The figure shows 5-minute average of the HOI to $I_2$ ratio and normalized signal of $HNO_3$ (1-min average). Note that the $I_2$ and HOI mixing ratios below the detection and quantification were omitted from the plot.

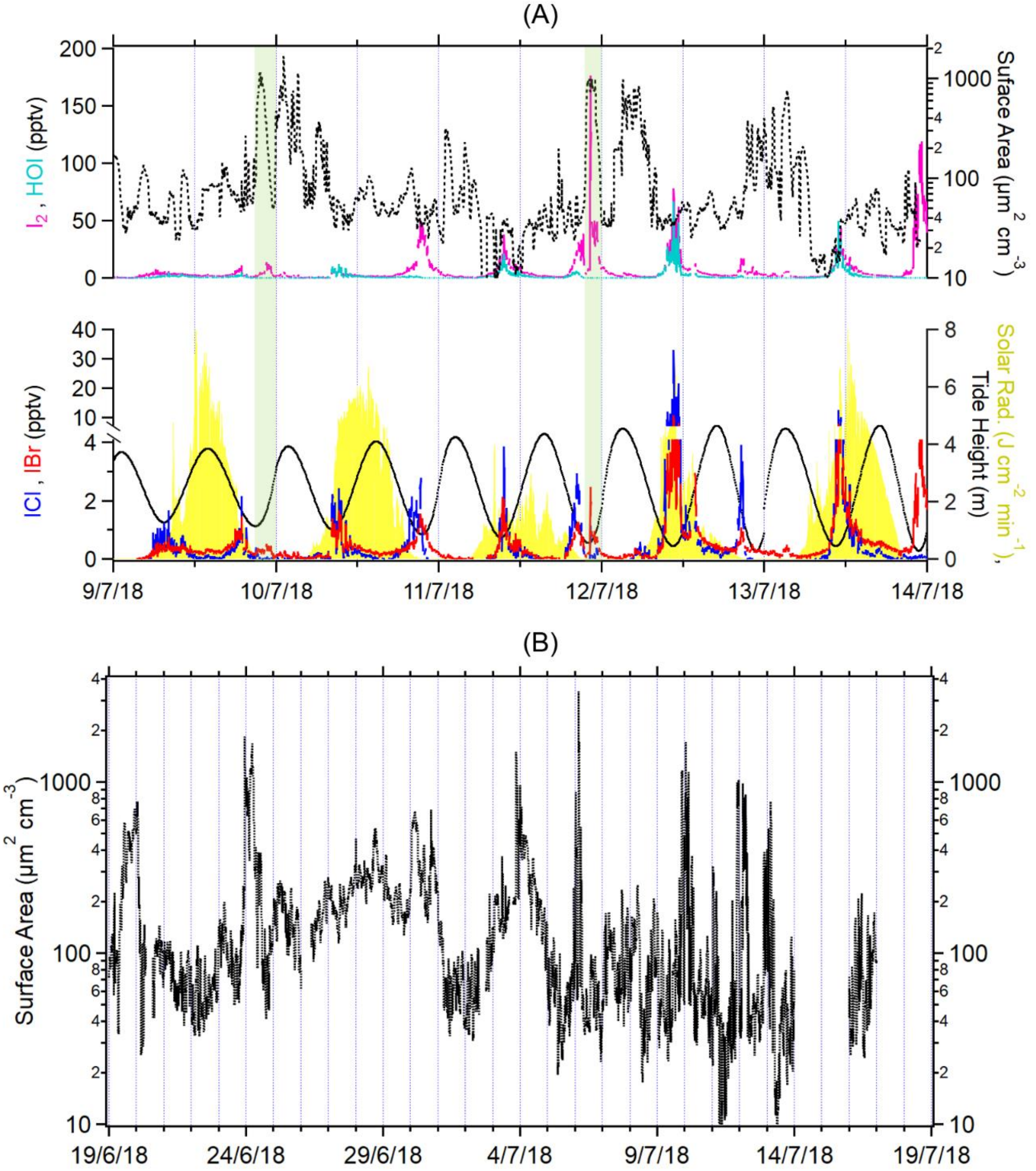

**Figure S2**. (A) An expanded view of the ICl and IBr mixing ratios, together with $I_2$, HOI, solar radiation, tide height, and aerosol surface area between July 09 and July 14, 2018. The green shaded areas show examples of iodine interhalogens peak at a nighttime low tide events. The gap between the data of $I_2$, HOI, ICl and IBr is mainly due to the operational switching between the measurements with bromide chemical ionization mode and natural ion mode. (B) Time series of aerosol surface area from June 19 to July 19, 2018. The missing period is due to the unavailability of particle measurement data.

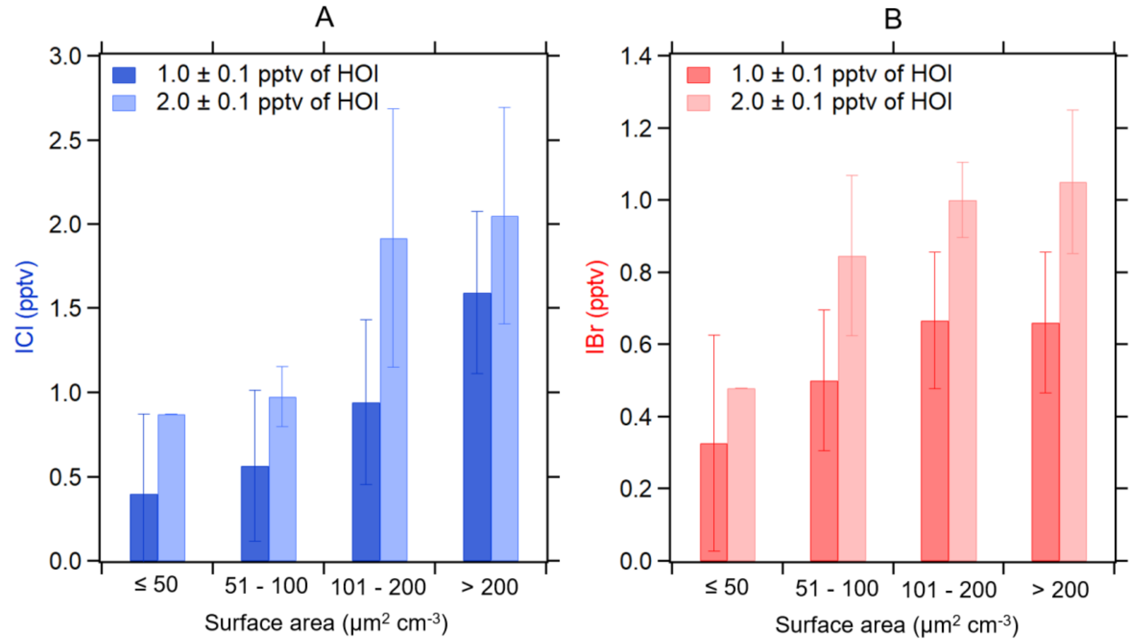

**Figure S3**. The average concentration of ICl (A) and IBr (B) with respect to different ranges of aerosol surface areas and HOI concentrations. It shows that ICl and IBr increase together with the aerosol surface area at a fixed HOI concentration of 1 pptv, and continue to increase when the HOI concentration reaches 2 pptv. The error bar is the standard deviation of the average concentration of ICl or IBr within the specific surface area-bin. For this analysis, only data at daytime low tides (tidal height < 2 m, and solar radiation > 0 J cm$^{-2}$ min$^{-1}$) from June 26 to July 14, 2018 were used.

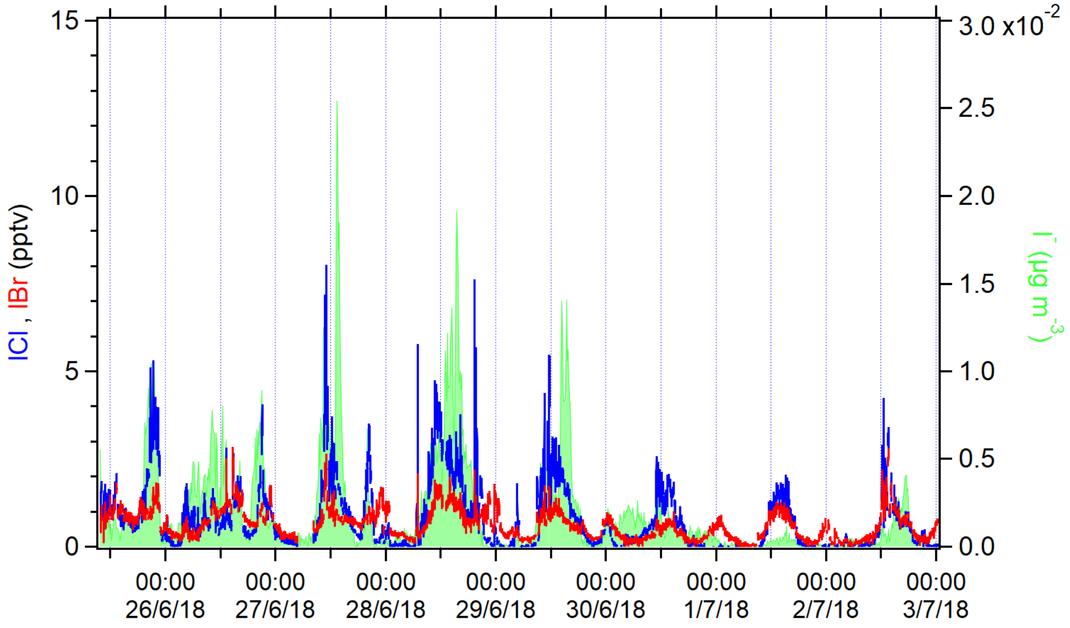

**Figure S4.** An expanded view of the time series for ICl and IBr from June 25 to July 3, 2018, and the corresponding iodide signal (not calibrated) measured by the aerosol mass spectrometer (AMS). The AMS was operated with an inlet with particle cut-off diameter of 1 micrometer.

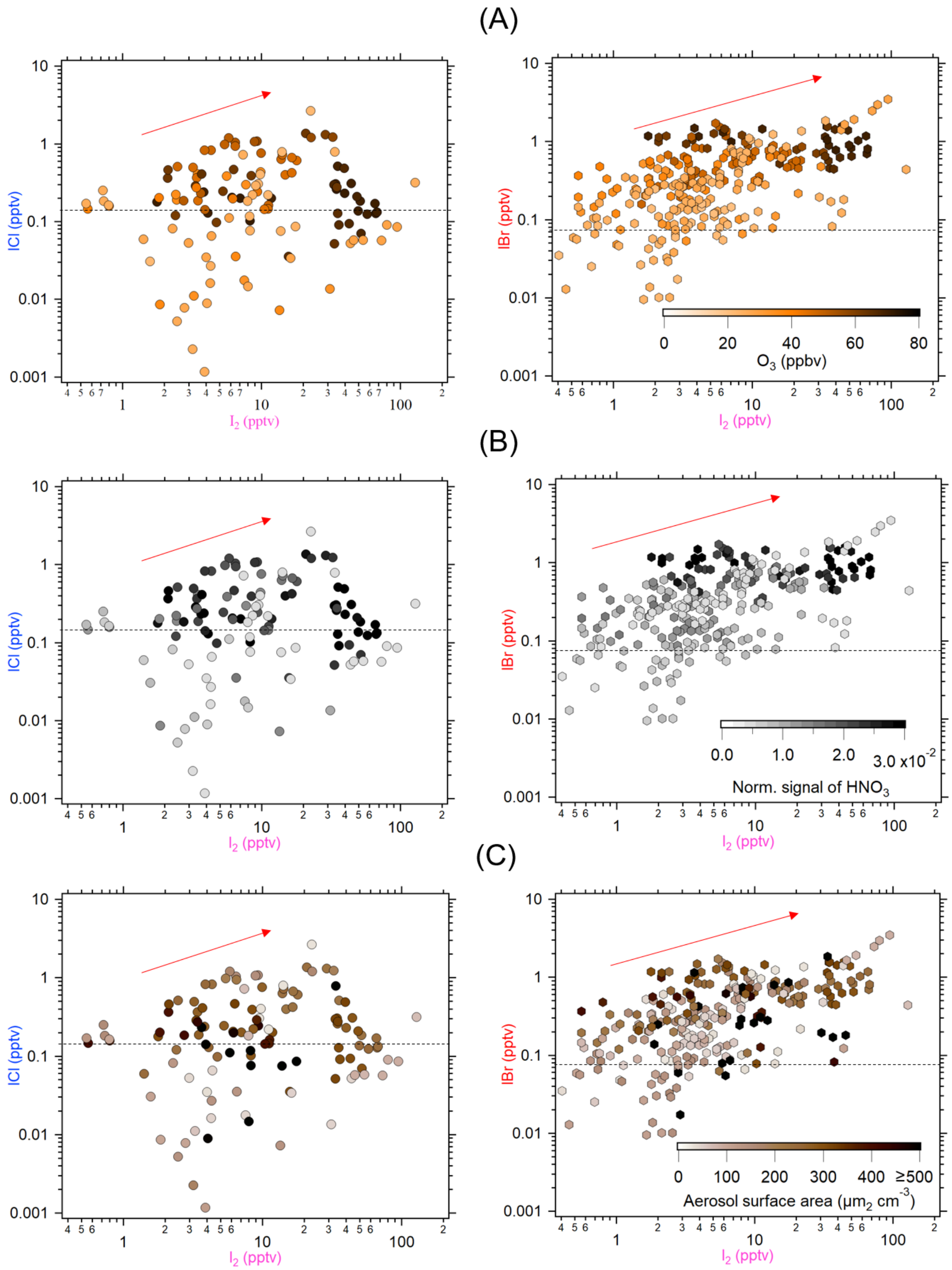

**Figure S5.** The IBr and ICl mixing ratios *vs.* $I_2$ mixing ratios during the nighttime low tides. The color codes represent the changes with: (A) $O_3$ concentration; (B) normalized signal of $HNO_3$, which is used here as proxy of the $NO_x$ level; and (C) the aerosol surface area. The black dash-line shows the LOD of ICl and IBr. The data is in 10-min averaged and background signal corrected. The negative values in the data were omitted from the plot. Note in plot (A), (B) and (C), when the concentrations of $I_2$, $O_3$, $HNO_3$ (not calibrated), and aerosol surface area are moving toward the higher end, the majority of the ICl and IBr are detected above the LODs, suggesting that the ICl and IBr are likely enhanced by the increase of $I_2$, $O_3$, $NO_x$ and aerosol surface area.

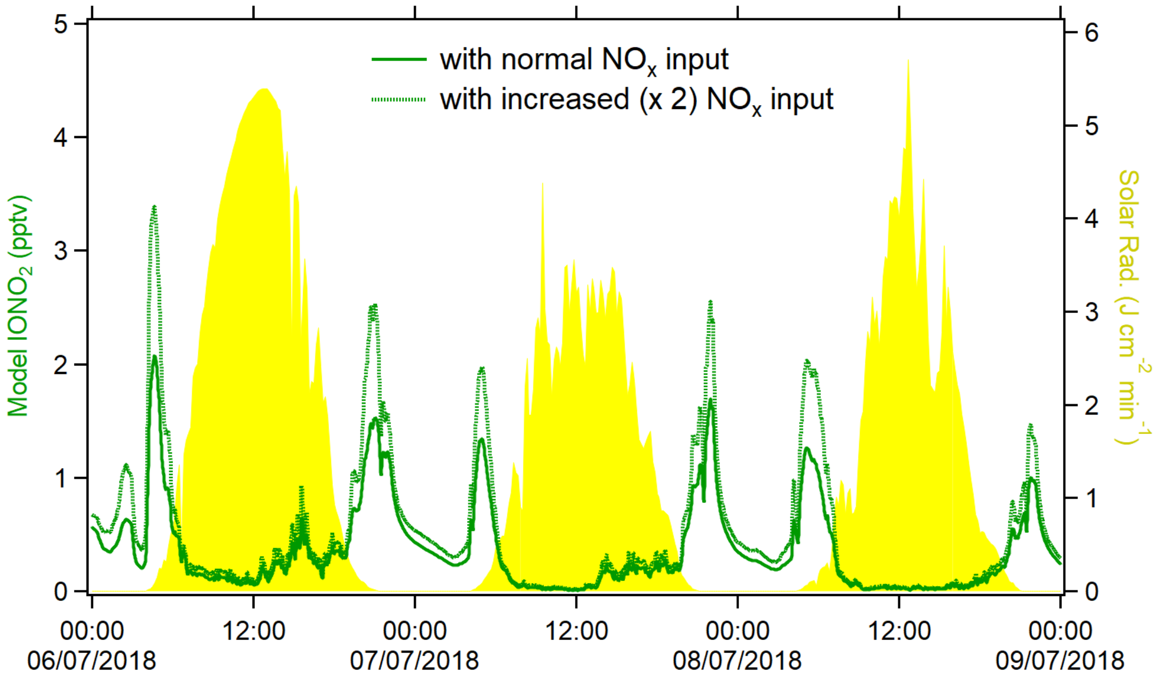

**Figure S6.** Example of model simulations of $IONO_2$ with different $NO_x$ concentrations (from simulation 2 and 4 in Table S7). The measured solar radiation is also depicted to show the $IONO_2$ diurnal variations.

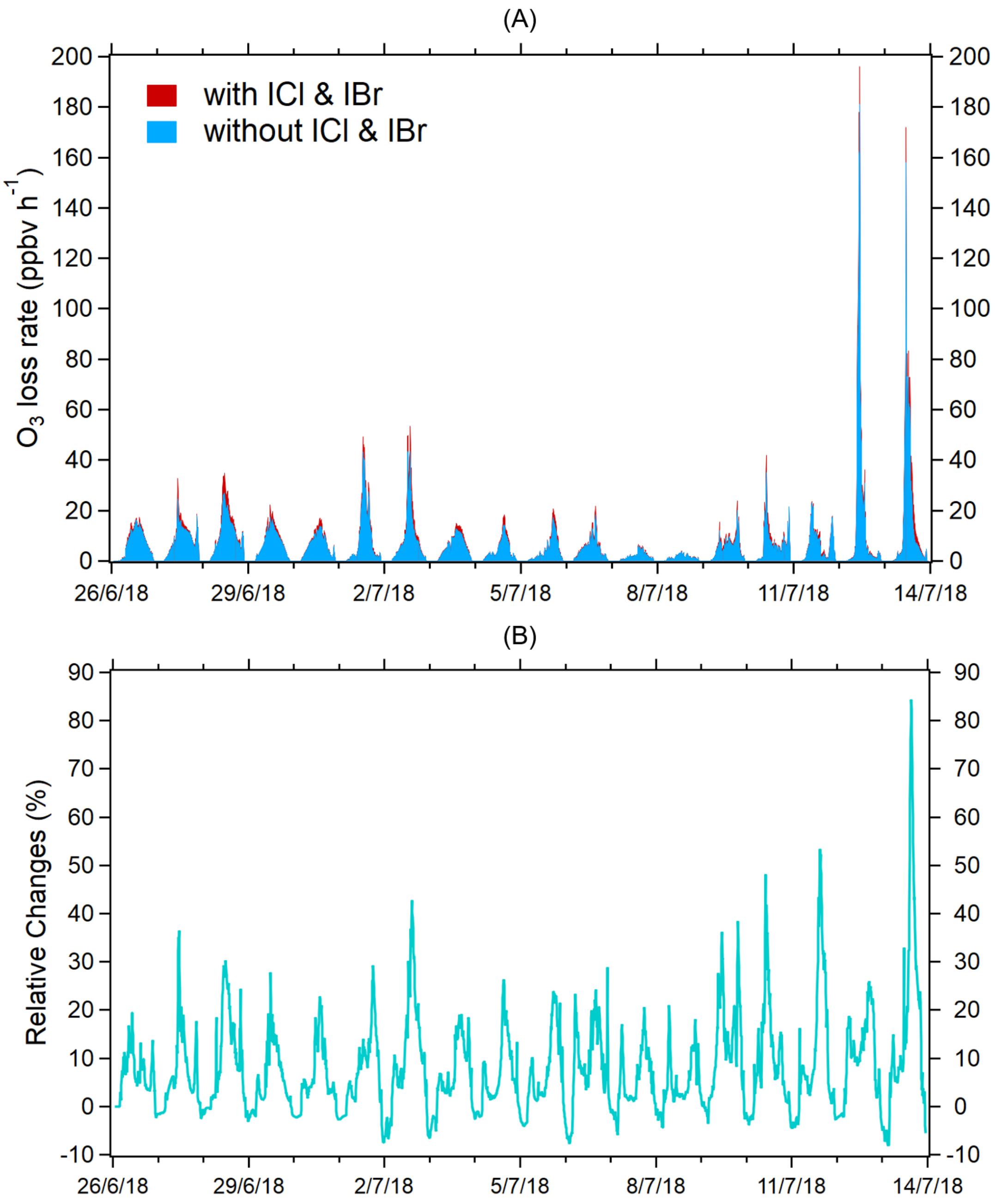

**Figure S7.** (A) The time series of $O_3$ loss rate calculated with and without constraining ICl and IBr into THAMO (Simulation 5 & 6 in Table S7). (B) The relative changes (%) of the $O_3$ loss rate with and without ICl and IBr.

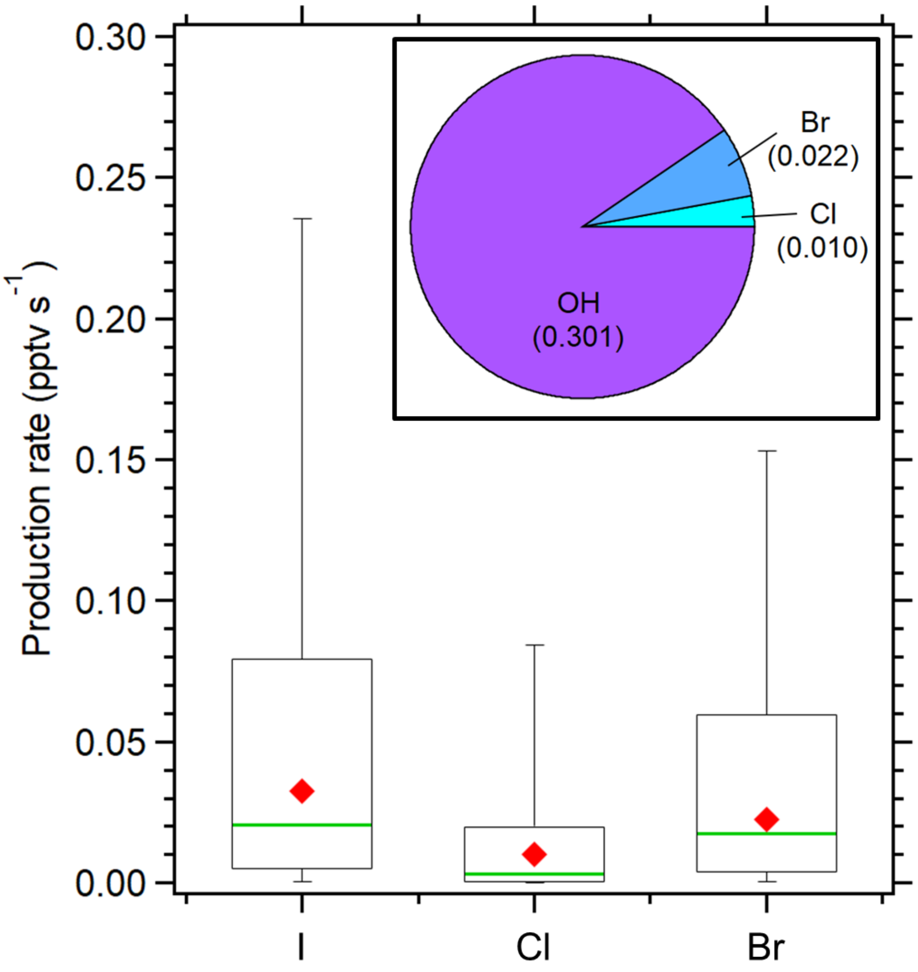

**Figure S8.** (A) The daytime production rates of iodine, chlorine and bromine atoms via photolysis of IBr and ICl in Mace Head. The red diamonds represent the mean value and the green solid lines are the median of the data set. The lower and upper limit of the box represents the 25 and 75 percentiles respectively, while the error bars are the 5 and 95 percentiles. (B) Pie chart shows the daytime production rate of the Cl (turquoise) and Br (sky blue) from photolysis of ICl and IBr in relative to the OH production rate (purple) obtained from the model with ICl and IBr constraints. The numbers in bracket are the production rate in pptv s$^{-1}$.

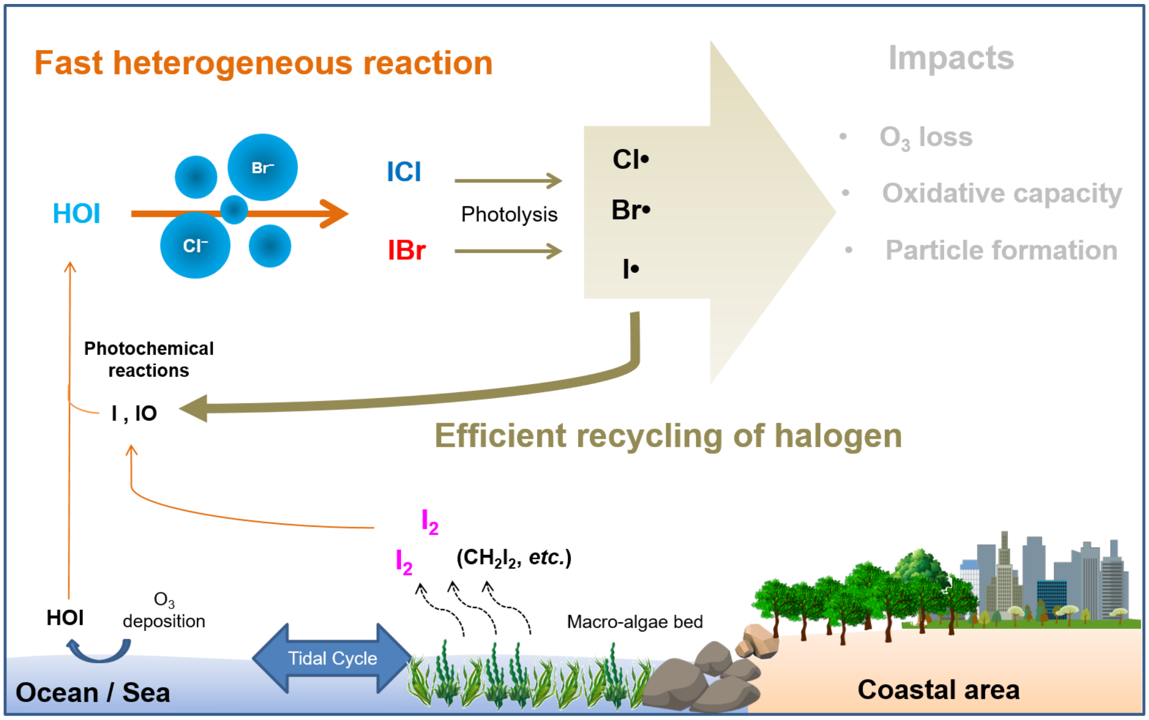

**Figure S9.** Schematic diagram of autocatalytic mechanisms of halogen release via heterogeneous process of HOI on marine aerosol and its potential impacts on the atmospheric chemistry and climate.

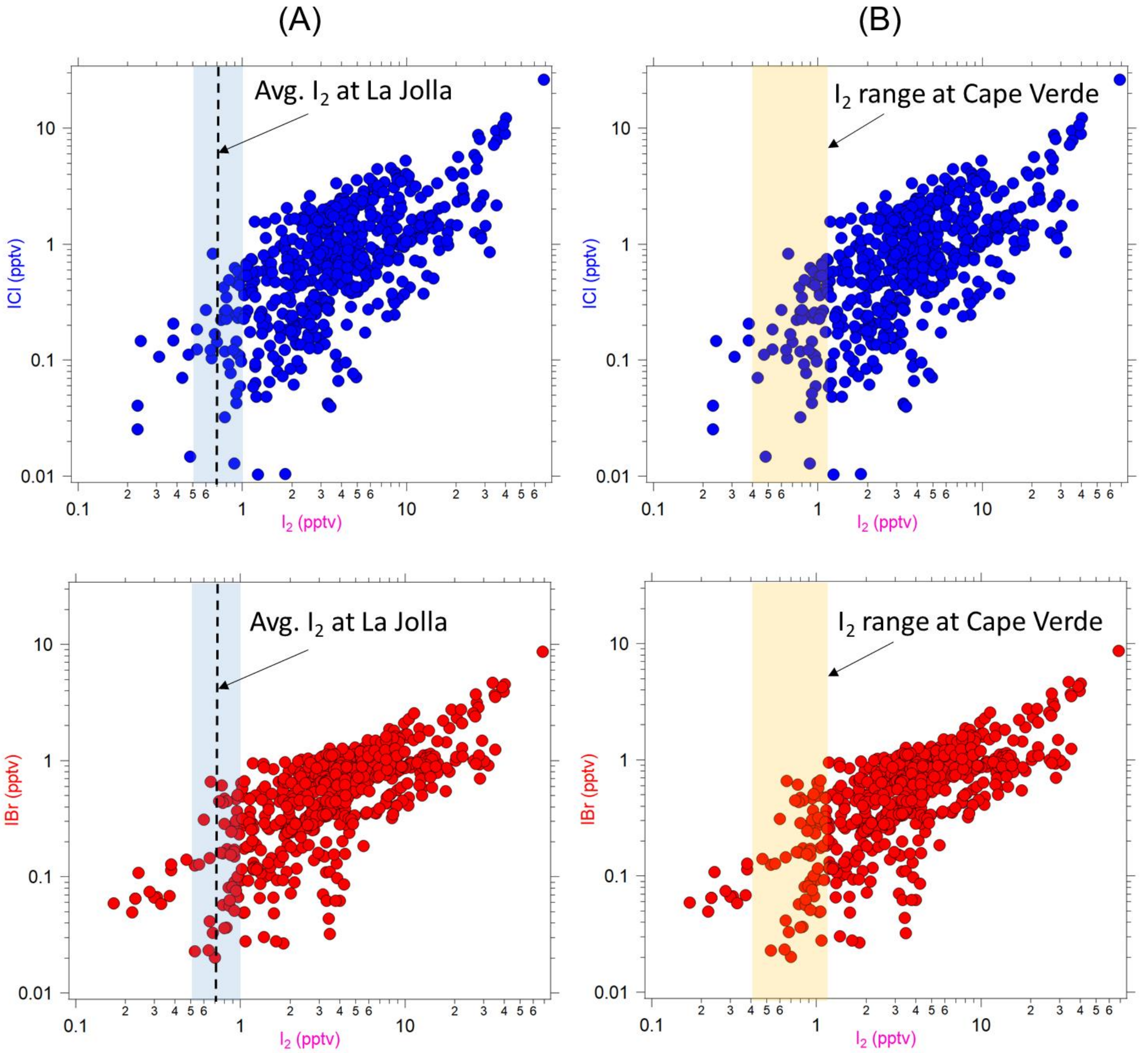

**Figure S10**. Plots for $I_2$ *vs.* ICl and IBr in our daytime low-tide measurement at Mace Head from June 26 to July 14, 2018. On the left panel (A), the black dash line is the average $I_2$ concentration, while the shaded blue area is the range of $I_2$ observed at La Jolla (32). On the right panel (B), the shaded yellow area represents the $I_2$ range observed at Cape Verde (49). Note that data below the LODs were removed in this analysis.

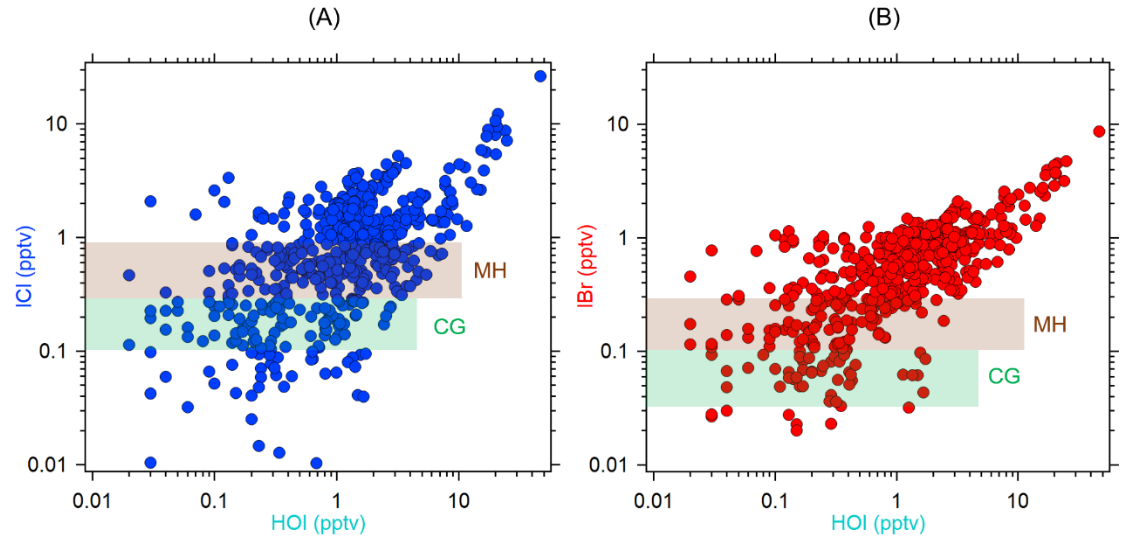

**Figure S11**. Plots of HOI *vs.* ICl (A) and IBr (B) from our daytime low-tide measurements at Mace Head from June 26 to July 14, 2018. The range of steady-state concentrations of daytime ICl and IBr at Mace Head (brown) and Cape Grim (green), calculated based on HOI heterogeneous uptake coefficient (lower γ = 0.3 and upper γ = 0.9), with similar HOI concentration, surface area, production yield, and photolysis rates of ICl and IBr as reported in McFiggans *et al.* (61).

**Figure S12.** The location of Mace Head atmospheric research station on the west coast of Ireland. Google map (blue box) shows an expanded view of the surrounding environment of Mace Head and nearby villages. Macroalgae bed being exposed to the air during a low tide event at Mace Head.

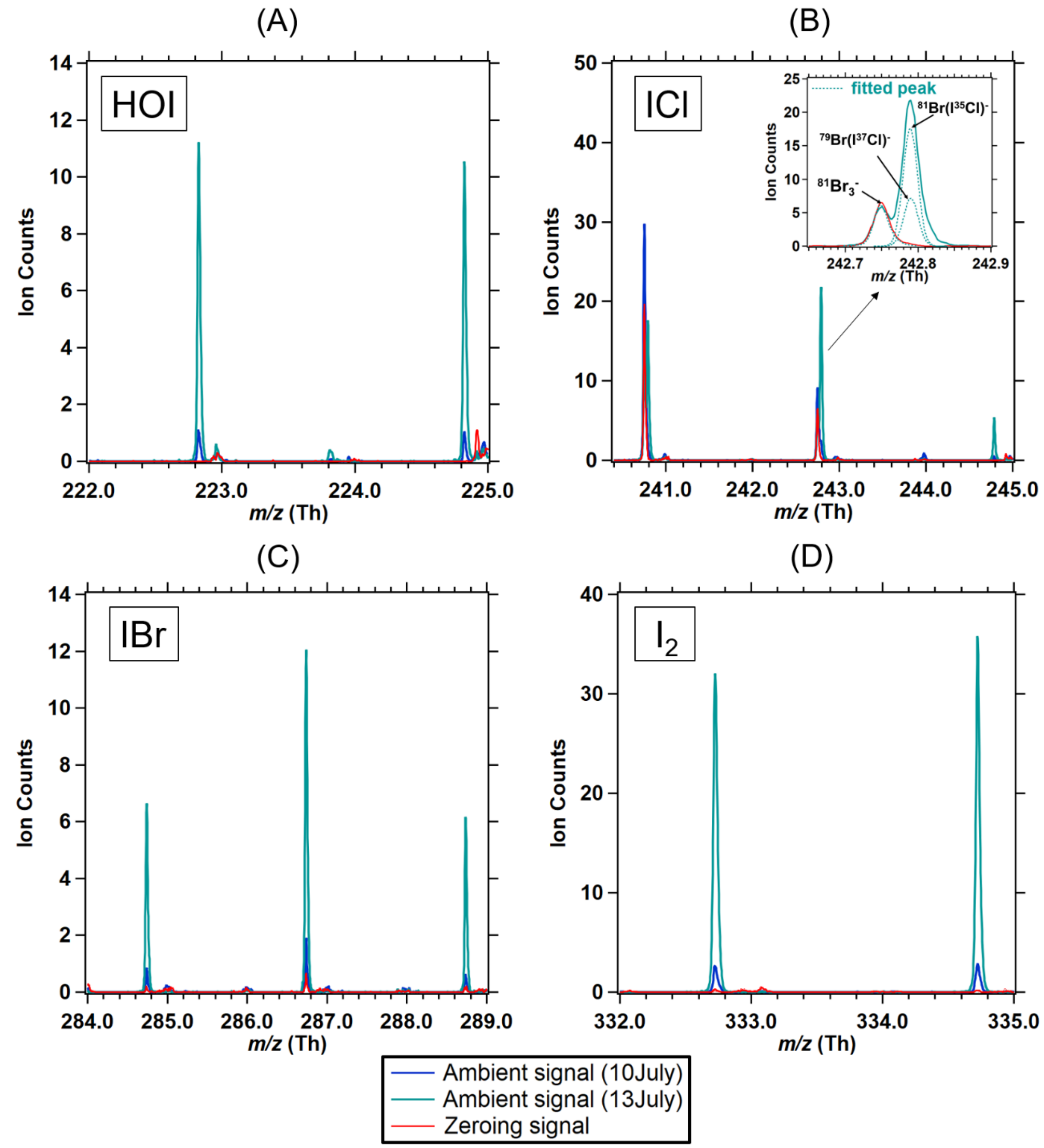

**Figure S13.** Comparison of high resolution peaks of halogen species in the ambient spectrum obtained on July 10, 2018 (blue), which represents a typical case; July 13, 2018 (cyan) representing an upper limit case; and a background zeroing measurement (red). (A) The $^{79}$Br(HOI)$^-$ peak at 222.8261 *m/z* and $^{81}$Br(HOI)$^-$ peak at 224.8241 *m/z*. (B) The peak of $^{79}$Br(I$^{35}$Cl)$^-$ at 240.7922 *m/z* with its respective isotopic peaks of $^{81}$Br(I$^{35}$Cl)$^-$ (242.7902 *m/z*), $^{79}$Br(I$^{37}$Cl)$^-$ (242.7893 *m/z*), $^{81}$Br(I$^{37}$Cl)$^-$ (244.7872 *m/z*). The isotopic peaks of Br$_3^-$ (*e.g.* $^{81}$Br$_3^-$ at 242.7494 *m/z*) are located next to the ICl peaks, inset figure shows an example that the high mass resolution of the instrument was able to distinguish these peaks. (C) The $^{79}$Br(I$^{79}$Br)$^-$ peak at 284.7414 *m/z* and $^{81}$Br(I$^{81}$Br)$^-$ at 288.7376 *m/z*. Note that the peaks of $^{81}$Br(I$^{79}$Br)$^-$ and $^{79}$Br(I$^{81}$Br)$^-$ cannot be separated due to their identical mass, therefore the signal at 286.7396 *m/z* is the sum of the two peaks. (D) The peak of $^{79}$Br(I$_2$)$^-$ at 332.7278 *m/z* and $^{81}$Br(I$_2$)$^-$ at 334.7258 *m/z*.

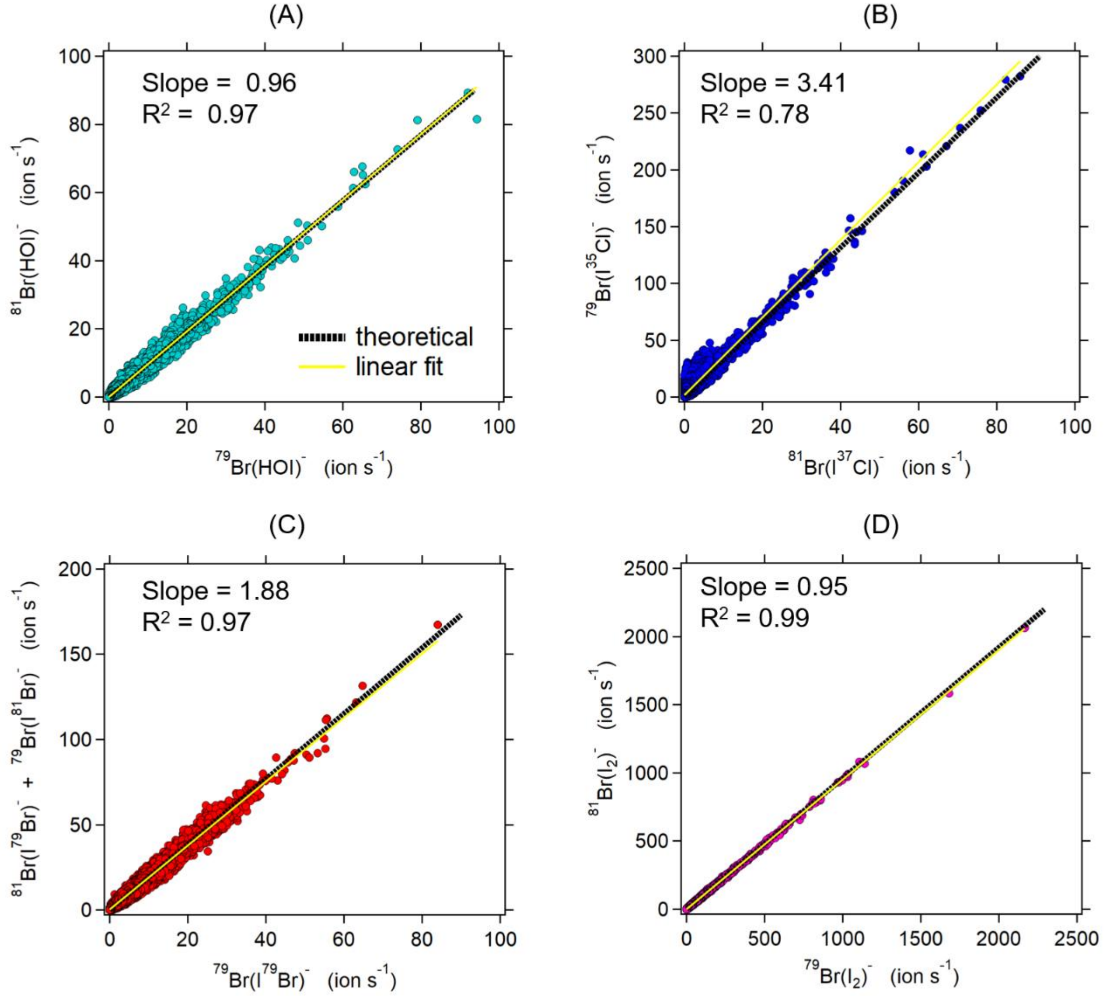

**Figure S14.** Scatter plots of the pre-averaged ambient signal (20s intervals) of halogen species and their isotopes over the entire campaign (June 19 – July 19, 2018): (A) $^{81}Br(HOI)^-$ *vs.* $^{79}Br(HOI)^-$; (B) $^{79}Br(I^{35}Cl)^-$ *vs.* $^{81}Br(I^{37}Cl)^-$; (C) $^{81}Br(I^{79}Br)^-$ + $^{79}Br(I^{81}Br)^-$ *vs.* $^{79}Br(I^{79}Br)^-$; and (D) $^{81}Br(I_2)^-$ *vs.* $^{79}Br(I_2)^-$. The yellow line is the linear fit of the data points ($N$ = 71840) to yield the slope and correlation coefficient ($R^2$). The black dash line is the theoretical slope. The accuracy of the observed *vs.* theoretical slope is within 9%.

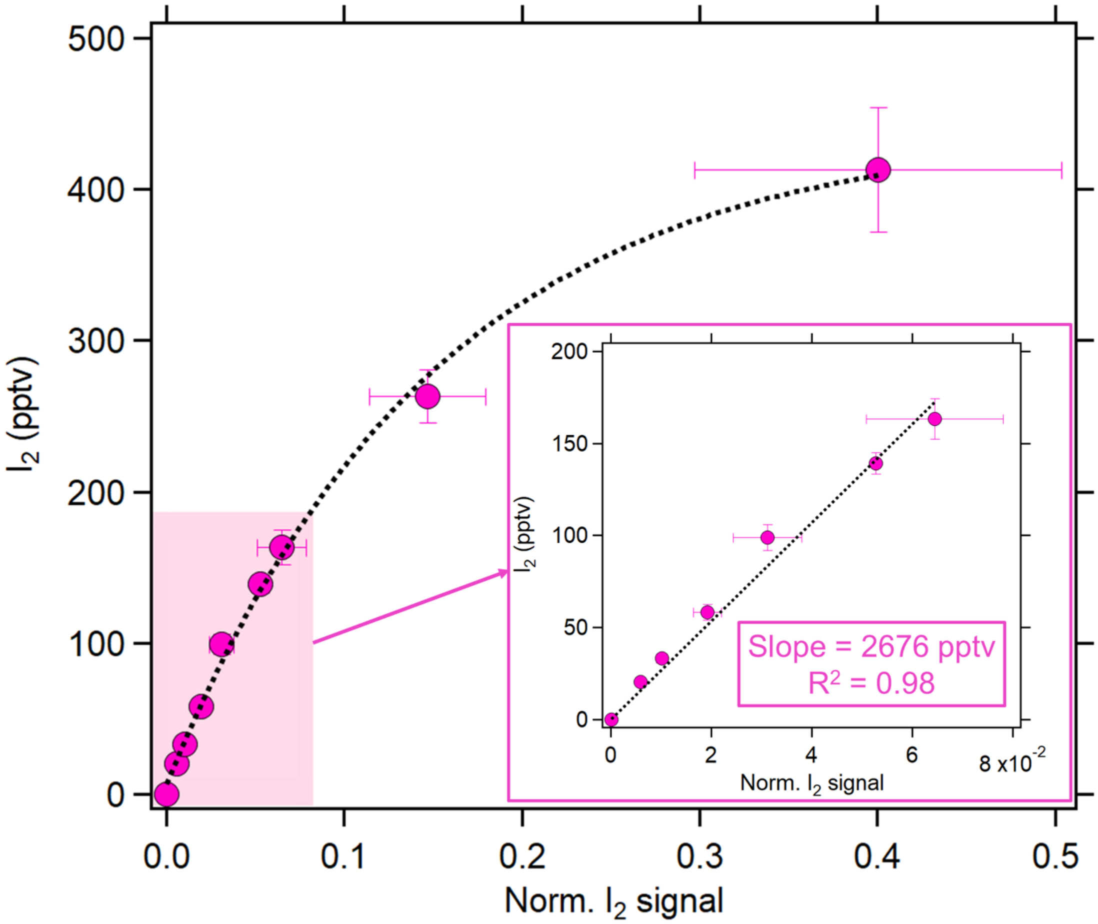

**Figure S15.** The plot of $I_2$ concentration *vs.* the normalized signal of $I_2$ detected by the Br-CI-APi-TOF. The solid pink circle is the average value from five different calibration experiments, while the black dash-line is the fitting line with intercept set at zero. The instrument shows a non-linear response to the high concentration of $I_2$, however, at lower $I_2$ concentration (*i.e.* < 180 pptv; shaded in pink), the instrument shows a linear response with a slope of 2676 pptv (see inset figure). The error bars are the standard deviation of the normalized $I_2$ signal obtained from five different calibration experiments (x-axis) and the uncertainty from the $I_2$ source (y-axis).

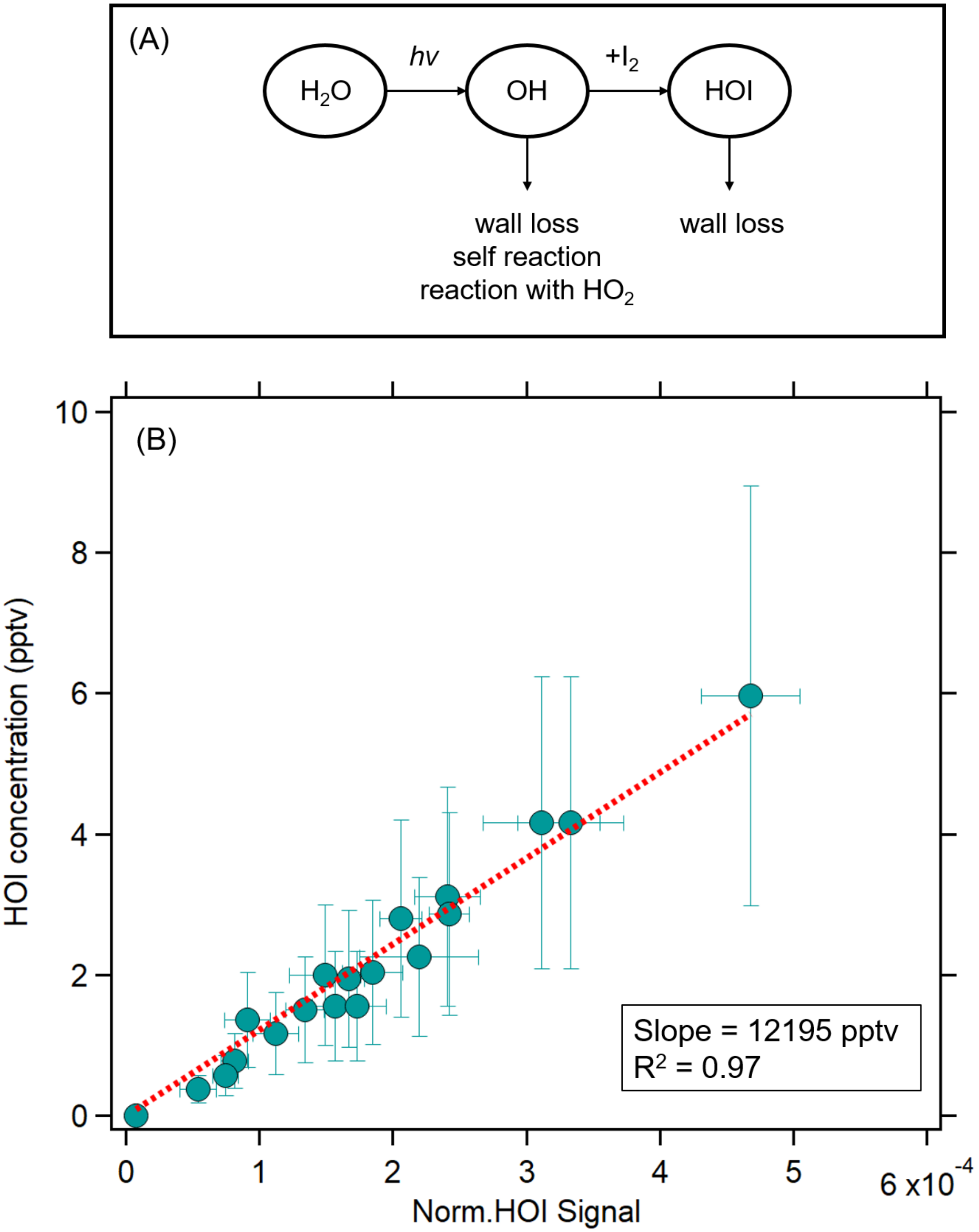

**Figure S16.** (A) Reaction scheme for modeling the HOI production in the calibration system. (B) The scatter plot of modeled HOI concentration *vs.* the normalized HOI signal (8-min average), obtained from three different HOI calibration experiments by varying the $I_2$ or OH concentration in the calibrator. The red dash-line is the linear-fitting with intercept set at zero. The error bar for x-axis represents the standard deviation from averaging over the 8-min data of the normalized HOI signal. The error bar for y-axis is the uncertainty of the modeled HOI concentration in the experiments.

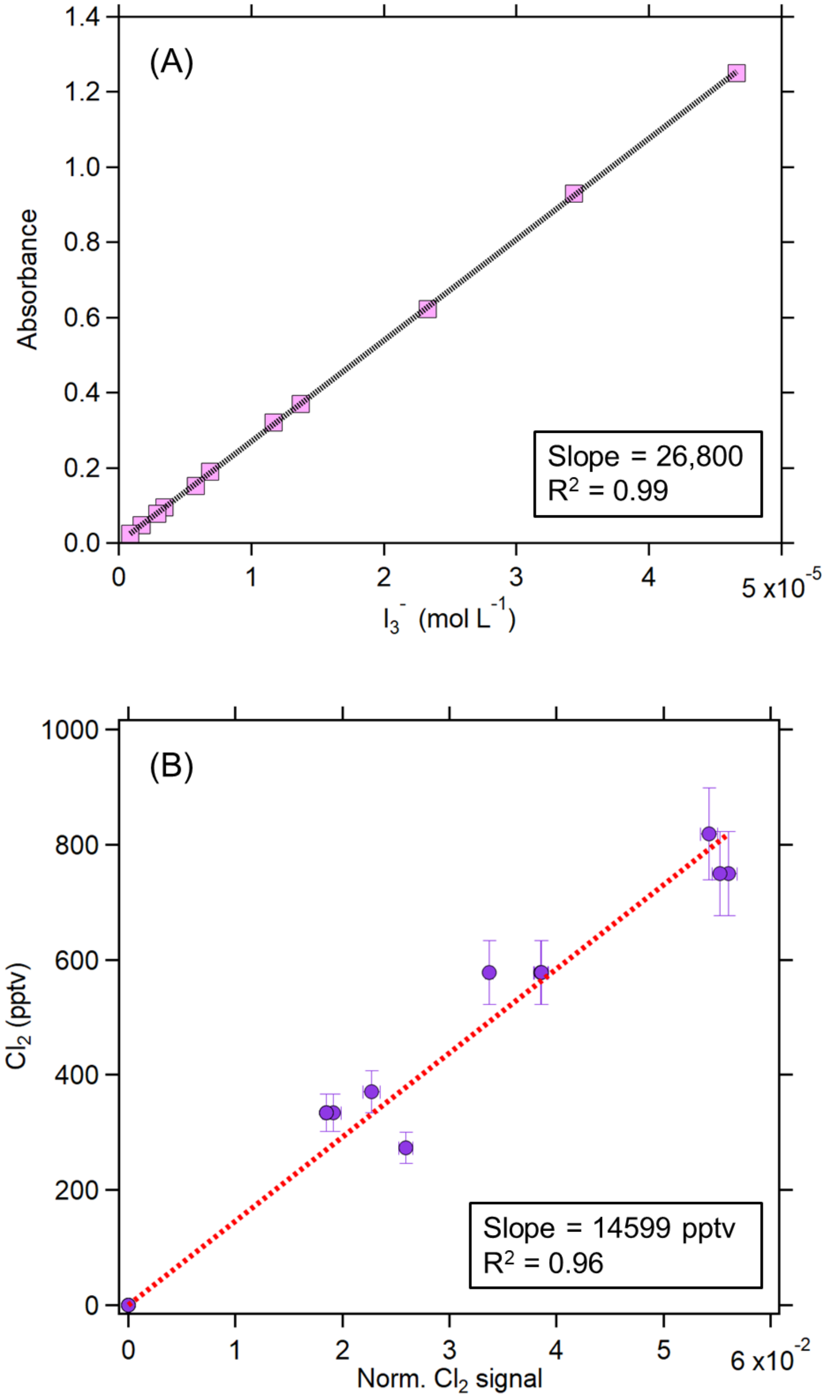

**Figure S17.** (A) The calibration plot made from different standard solutions for $I_3^-$ at 352 nm. Black dash-line is the linear-fitting of the data. (B) Scatter plot for the $Cl_2$ concentration *vs.* the normalized $Cl_2$ signal (5-min average) from three different calibration experiments. The red dash-line is the linear-fitting with intercept set at zero. The error bar represents the standard deviation of the averaging over 5 min of data intervals (x-axis) and the uncertainty from the $Cl_2$ source (y-axis). The experiments were conducted at room temperature and under humidified inlet flow (relative humidity was ~25%).

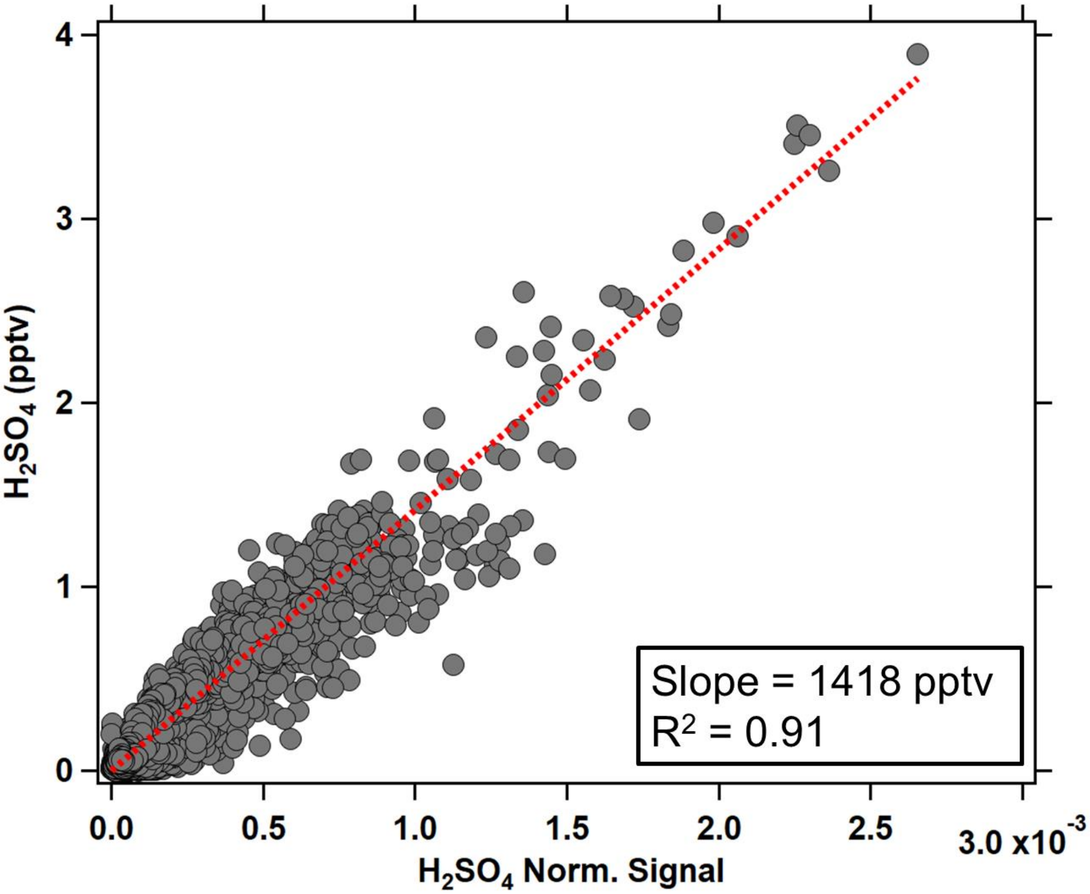

**Figure S18.** The response of the normalized signals of $H_2SO_4$ from the Br-Api-TOF *vs.* the changes of ambient $H_2SO_4$ measured by the nitrate-CIMS (1 min-average data) over the entire campaign, June 19 to July 19, 2018 (*N* = 25993). Note that the nitrate-CIMS measurement was offline from 15:00 June 22, 2018 to 14:00 July 4, 2018 (UTC) due to instrumentation problem. The red dash-line is the linear-fitting with intercept set at zero.

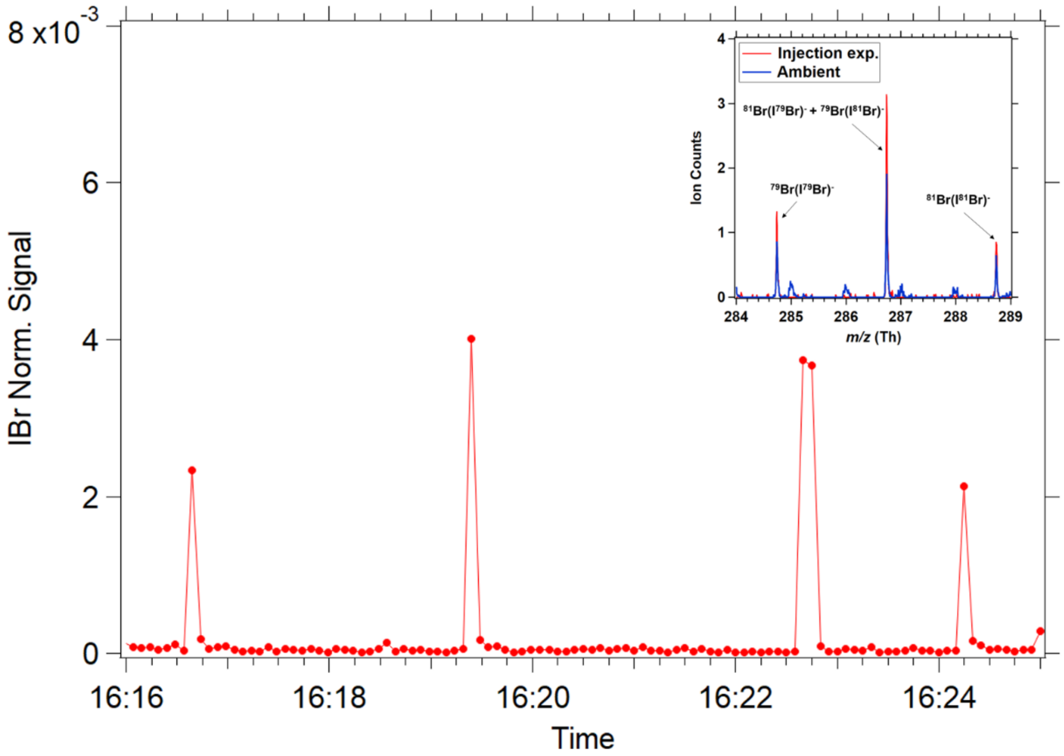

**Figure S19**. The response of the instrument (Br-CI-APi-TOF) to each injection of IBr-laden $N_2$ gas. Each data point is 5 s average interval. The inset figure shows the comparison of the IBr peaks measured in the ambient air and from the injection experiments.

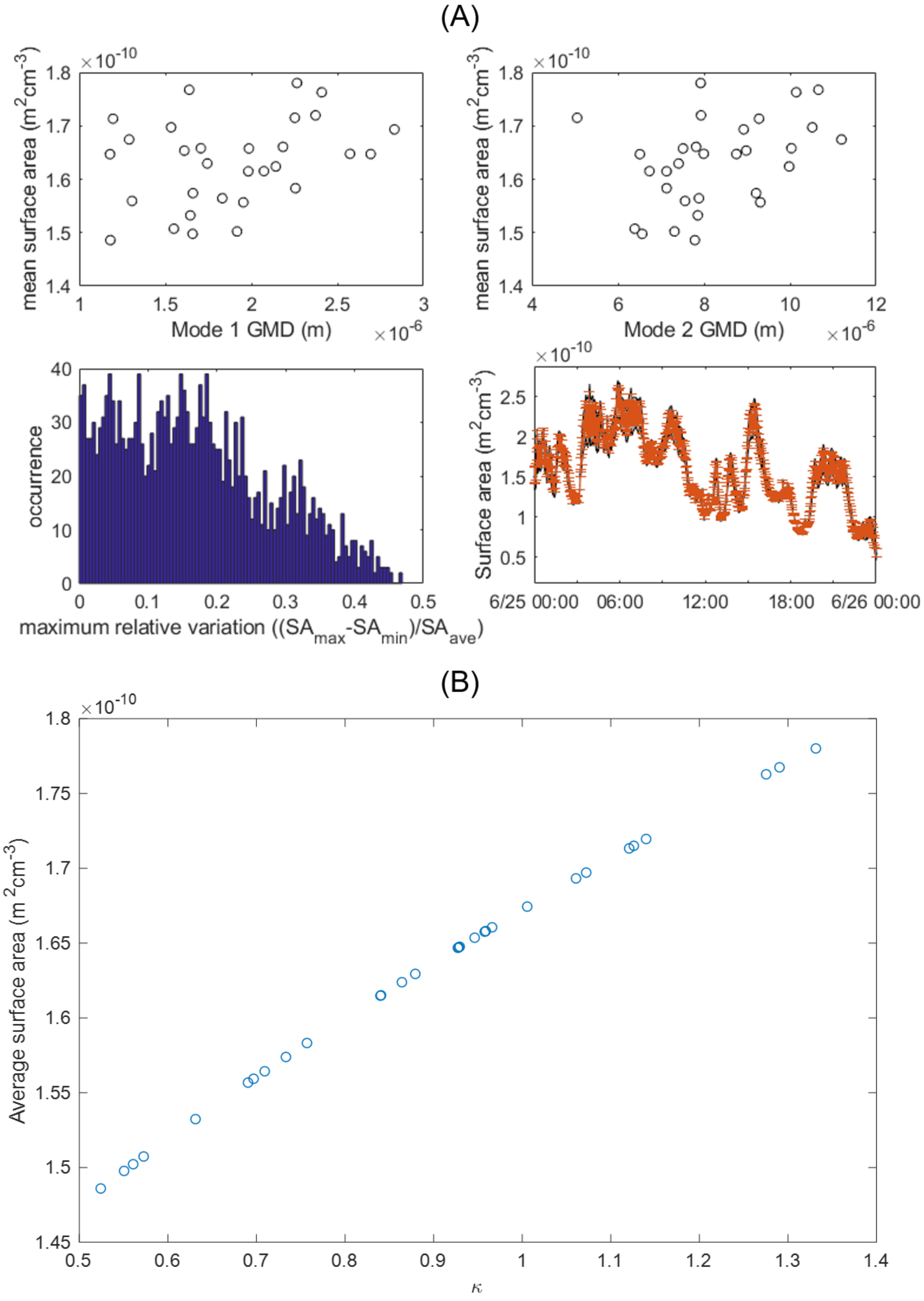

**Figure S20**. (A) Upper panels: the obtained surface area when varying the peak positions of the supermicron mass distribution around 2.0 microns (left) and 8.0 microns (right). Lower left: the maximum relative variation obtained from varying the peak positions and $\kappa$. Lower right: an example from the time series with the variation shown. (B) The average surface area obtained by varying input parameters, as a function of the $\kappa$ parameter.

**Table S1**. Summary of heterogeneous uptake coefficient of HOI (γ) on sea-salt/halides surfaces obtained from laboratory studies (62).

| **Substrate** | **Conditions** | | | | **Uptake coefficient (γ)** | ***Ref.*** |
|---|---|---|---|---|---|---|
| | **RH** | **Surface** | **T** | **P** | | |
| **sea-salt/aged** | 0-23% | Coated-thin film | 278 and 298 K | 1.2 – 3.5 Torr | 0.014 | Mossinger and Cox (63) |
| **sea-salt/fresh** | 0-23% | Coated-thin film | 278 and 298 K | 1.2 – 3.5 Torr | 0.061 | Mossinger and Cox (63) |
| **$Cl^-$ / $Br^-$** | dry | salt surfaces | 243, 253 or 298 K | 1 – 3 Torr | > 0.01 | Holmes et al. (64) |
| **$Cl^-$ / $Br^-$** | *N/A* | aqueous solutions (wetted-wall) | 274 K | 5 – 20 Torr | 0.0022 | Braban et al. (65) |

*N/A = information not available*

**Table S2**. The diffusion coefficient of various halogen species in $N_2$/air and their estimated diffusion time to the inlet wall.

| **Molecule** | **Diffusion coefficient ($cm^2$ $s^{-1}$) in $N_2$ or (air)** | ***Ref.*** | **Diffusion time to inlet wall, *x* = 1.2 cm (inlet r.t. = 1.8 s)** |
|---|---|---|---|
| $I_2$ | 0.070 | Tang et al. (15)<br>Gu et al. (16) | 10.2 s |
| $Br_2$ | 0.106 (in air) | Lugg (66) | 6.8 s |
| $Cl_2$ | 0.124 (in air) | Andrew (67) | 5.8 s |
| HOI | 0.122 | Calculated with Fuller's method* | 5.9 s |
| HOBr | 0.121 | Fickert et al. (68) | 6.0 s |
| HOCl | 0.153 | Calculated with Fuller's method* | 4.7 s |
| ICl | 0.109 | Calculated with Fuller's method* | 6.6 s |
| IBr | 0.106 | Calculated with Fuller's method* | 6.8 s |
| BrCl | 0.120 | Calculated with Fuller's method* | 6.0 s |

**as shown in Tang et al. (15)*
*r.t. = residence time*

**Table S3.** Cluster formation energy of different species with bromide anion and their corresponding calibration factor determined in the laboratories. The reaction enthalpies of formation pathways that can possibly affect the formations or losses of the ICl and IBr are also presented.

| **Formation pathway** | **Cluster formation enthalpies (kcal mol$^{-1}$)** | **Calibration coefficient (pptv)** |
|---|---|---|
| *Main* | | |
| $H_2SO_4 + Br^- \rightarrow H_2SO_4.Br^-$ | −41.1 | 1418 |
| $IBr + Br^- \rightarrow IBr \cdot Br^-$ | −36.7 | 1418[a] |
| $ICl + Br^- \rightarrow ICl \cdot Br^-$ | −33.8 | 1418[a] |
| $I_2 + Br^- \rightarrow I_2 \cdot Br^-$ | −33.7 | 2676 |
| $Cl_2 + Br^- \rightarrow Cl_2 \cdot Br^-$ | −22.3 | 14599 |
| $HOI + Br^- \rightarrow HOI \cdot Br^-$ | −26.9 | 12195 |
| | | |
| *Other* | | |
| **Formation pathway** | **Reaction enthalpies (kcal mol$^{-1}$)** | |
| $ICl + Br^- \rightarrow IBr + Cl^-$ | +6.0 | |
| $ICl + Br^- \rightarrow BrCl + I^-$ | +8.2 | |
| $I_2 + Br^- \rightarrow IBr + I^-$ | +7.9 | |
| $IBr + Br^- \rightarrow Br_2 + I^-$ | +2.7 | |

[a] *calibration coefficient similar to the $H_2SO_4$ is used for this species*

**Table S4.** Summary of key measurements and instruments in Mace Head relevant to this study.

| **Instrument** | **Parameters** | **Model** |
|---|---|---|
| *Gas* | | |
| Bromide CI-API-TOF | $I_2$, HOI, ICl, IBr, $H_2SO_4$, $HNO_3$ (uncalibrated) | Karsa/Aerodyne |
| $O_3$ analyzer | $O_3$ | Thermo Scientific, model 49i |
| CO analyzer | CO | Trace Analytical RGA3 |
| Nitrate – Chemical Ionization Mass Spectrometer (CIMS) | $H_2SO_4$ | Mauldin III *et al.* (35) |
| *Aerosol* | | |
| $PM_{2.5}$ | $PM_{2.5}$ | TEOM model 1405 |
| $PM_{10}$ | $PM_{10}$ | TEOM model 1405 |
| SMPS | Size distribution of particles between 20 and 550 nm | 20-500, Vienna type DMA, TSI 3010 CPC |
| Aerosol Mass Spectrometer | $SO_4^{2-}$ and $I^-$ in $PM_1$ | Aerodyne HR-ToF-AMS |
| *Meteorology* | | |
| Temperature and RH sensor | RH and Temperature | Platinum Resistance Thermometers PRT's Sensing Devices Pt100<br>RH Vaisala HMP 45D, 243, 155 |
| Wind sensor | Wind direction and speed | Wind Vector A100L2 Anemometer W200P Windvane |
| Solar radiation | Solar radiation | Kipp & Zonen CMP11 |

**Table S5**. Chemical reactions embedded in the THAMO model (46).

| **Bimolecular Reactions** | **Bimolecular Rate Constants ($cm^3$ $molecule^{-1}$ $s^{-1}$)** |
|---|---|
| B1. $O(^1D) + N_2 \rightarrow O + N_2$ | $1.8 \times 10^{-11} \times e^{(110 / T)}$ |
| B2. $O(^1D) + O_2 \rightarrow O + O_2$ | $3.2 \times 10^{-11} \times e^{(70 / T)}$ |
| B3. $O(^1D) + H_2O \rightarrow OH + OH$ | $2.2 \times 10^{-10}$ |
| B4. $O(^1D) + CH_4 \rightarrow CH_3 + OH$ (0.75), $CH_3O + H$ (0.2), $HCHO + H_2$ (0.05) | $1.5 \times 10^{-10}$ |
| B5. $O(^1D) + H_2 \rightarrow OH + H$ | $1.1 \times 10^{-10}$ |
| B6. $OH + CO \rightarrow H + CO_2$ | $1.5 \times 10^{-13} \times (1 + 0.6 \times P_{atm})$ |
| B7. $HO_2 + NO \rightarrow NO_2 + OH$ | $3.5 \times 10^{-12} \times e^{(250 / T)}$ |
| B8. $O_3 + HO_2 \rightarrow OH + 2O_2$ | $1.1 \times 10^{-14} \times e^{(-500 / T)}$ |
| B9. $HO_2 + HO_2 \rightarrow H_2O_2 + O_2$ | $2.3 \times 10^{-13} \times e^{(600 / T)}$ |
| B10. $OH + H_2 \rightarrow H_2O + H$ | $5.5 \times 10^{-12} \times e^{(-2000 / T)}$ |
| B11. $O_3 + OH \rightarrow HO_2 + O_2$ | $1.6 \times 10^{-12} \times e^{(-940 / T)}$ |
| B12. $OH + HNO_3 \rightarrow H_2O + NO_3$ | $k_0 = 7.2 \times 10^{-15} \times e^{(785 / T)}$<br>$k_2 = 4.1 \times 10^{-16} \times e^{(1440 / T)}$<br>$k_3 = 1.9 \times 10^{-33} \times e^{(725 / T)}$<br>$k=k_0+(k_3 x[M]/(1+k_3x[M]/k_2))$ |
| B13. $H_2O_2 + OH \rightarrow H_2O + HO_2$ | $2.9 \times 10^{-12} \times e^{(-160 / T)}$ |
| B14. $OH + HO_2NO_2 \rightarrow NO_2 + HO_2 + OH$ | $1.3 \times 10^{-12} \times e^{(380 / T)}$ |
| B15. $OH + HO_2 \rightarrow H_2O + O_2$ | $4.8 \times 10^{-11} \times e^{(250 / T)}$ |
| B16. $OH + HONO \rightarrow H_2O + NO_2$ | $1.8 \times 10^{-11} \times e^{(390 / T)}$ |
| B17. $C_2H_5 + O_2 \rightarrow C_2H_4 + HO_2$ | $2 \times 10^{-14}$ |
| B18. $OH + CH_4 \rightarrow CH_3 + H_2O$ | $2.45 \times 10^{-12} \times e^{(-1775 / T)}$ |
| B19. $O(^3P) + CH_3 \rightarrow CH_3O$ | $1.1 \times 10^{-10}$ |
| B20. $CH_3O_2 + HO_2 \rightarrow CH_3OOH + O_2$ | $3.8 \times 10^{-13} \times e^{(800 / T)}$ |
| B21. $CH_3OOH + OH \rightarrow CH_3(O)O + H_2O$ | $0.7 \times 3.8 \times 10^{-12} \times e^{(200 / T)}$ |
| B22. $CH_3O + O_2 \rightarrow CH_2O + HO_2$ | $3.9 \times 10^{-14} \times e^{(-900 / T)}$ |
| B23. $OH + HCHO \rightarrow H_2O + HCO$ | $8.8 \times 10^{-12} \times e^{(25 / T)}$ |
| B24. $HCO + O_2 \rightarrow CO + HO_2$ | $3.5 \times 10^{-12} \times e^{(140 / T)}$ |
| B25. $CH_3O_2 + CH_3O_2 \rightarrow 2CH_3O + O_2$ (0.29) | $0.29 \times 2.5 \times 10^{-13} \times e^{(190 / T)}$ |
| B26. $NO + CH_3O_2 \rightarrow NO_2 + CH_3O$ | $3 \times 10^{-12} \times e^{(280 / T)}$ |
| B27. $NO + O_3 \rightarrow NO_2 + O_2$ | $2 \times 10^{-12} \times e^{(-1400 / T)}$ |
| B28. $NO + NO_3 \rightarrow 2NO_2$ | $1.5 \times 10^{-11} \times e^{(170 / T)}$ |
| B29. $NO_3 + HCHO \rightarrow$ Products | $5.8 \times 10^{-16}$ |
| B30. $HO_2 + SO_2 \rightarrow$ Products | $1 \times 10^{-18}$ |
| B31. $N_2O_5 + H_2O \rightarrow 2HNO_3$ | $2.5 \times 10^{-22}$ |
| B32. $NO_2 + O_3 \rightarrow NO_3 + O_2$ | $1.2 \times 10^{-13} \times e^{(-2450 / T)}$ |
| B33. $OH + O(^3P) \rightarrow H + O_2$ | $2.2 \times 10^{-11} \times e^{(120 / T)}$ |
| B34. $O(^3P) + HO_2 \rightarrow OH + O_2$ | $3 \times 10^{-11} \times e^{(200 / T)}$ |
| B35. $H_2O_2 + O(^3P) \rightarrow OH + HO_2$ | $1.4 \times 10^{-12} \times e^{(-2000 / T)}$ |
| B36. $OH + OH \rightarrow H_2O + O(^3P)$ | $4.2 \times 10^{-12} \times e^{(-240 / T)}$ |
| B37. $O_3$ + Alkenes $\rightarrow$ Products | $1.2 \times 10^{-14} \times e^{(-2630 / T)}$ |
| B38. $NO_3 + CO \rightarrow$ Products | $4 \times 10^{-19}$ |
| B39. $OH + CH_3OOH \rightarrow CH_2OOH + H_2O \rightarrow CH_2O + OH + H_2O$ | $0.3 \times 3.8 \times 10^{-12} \times e^{(200 / T)}$ |
| B40. $O(^3P) + HCHO \rightarrow OH + HCO$ | $3.4 \times 10^{-11} \times e^{(-1600 / T)}$ |
| B41. $H_2S + NO_3 \rightarrow$ Products | $8 \times 10^{-16}$ |
| B42. $HCHO + HO_2 \rightarrow HO_2CH_2O$ | $6.7 \times 10^{-15} \times e^{(600 / T)}$ |
| B43. $H + O_3 \rightarrow OH + O_2$ | $1.4 \times 10^{-10} \times e^{(-470 / T)}$ |
| B44. $HO_2 + H \rightarrow 2OH$ | $0.9 \times 8.1 \times 10^{-11}$ |
| B45. $O(^3P) + HO_2NO_2 \rightarrow$ Products | $7.8 \times 10^{-11} \times e^{(-3400 / T)}$ |
| B46. $O(^1D) + O_3 \rightarrow 2O_2$ | $1.2 \times 10^{-10}$ |
| B47. $O(^1D) + O_3 \rightarrow O_2 + 2O$ | $1.2 \times 10^{-10}$ |
| B48. $CH_3O_2 + SO_2 \rightarrow$ Products | $5 \times 10^{-17}$ |
| B49. $NO_3 + HO_2 \rightarrow OH + NO_2 + O_2$ | $3.5 \times 10^{-12}$ |
| B50. $CH_3 + O_3 \rightarrow$ Products | $5.4 \times 10^{-12} \times e^{(-220 / T)}$ |
| B51. $H_2S + OH \rightarrow SH + H_2O$ | $6 \times 10^{-12} \times e^{(-75 / T)}$ |

| | |
|---|---|
| B52. $SO_2 + O_3 \rightarrow SO_3 + O_2$ | 3 x $10^{-12}$ x $e^{(-7000 / T)}$ |
| B53. $NO_3 + OH \rightarrow NO_2 + HO_2$ | 2.2 x $10^{-11}$ |
| B54. $O_3 + O(^3P) \rightarrow 2O_2$ | 8 x $10^{-12}$ x $e^{(-2060 / T)}$ |
| B55. $O_3 + HONO \rightarrow O_2 + HNO_3$ | 5 x $10^{-19}$ |
| B56. $CH_3O_2 + O_3 \rightarrow$ Products | 3 x $10^{-17}$ |
| B57. $NO_3$ + Alkenes $\rightarrow HOCH_2CH_2 + NO_2$ | 3 x $10^{-14}$ |
| B58. $SO_2 + NO_2 \rightarrow$ Products | 2 x $10^{-26}$ |
| B59. $NO_3$ + Alkanes $\rightarrow C_2H_5 + HNO_3$ | 3.6 x $10^{-17}$ |
| B60. $CH_3O_2 + CH_3O_2 \rightarrow CH_2O + CH_3OH + O_2$ | 0.71 x 2.5 x $10^{-13}$ x $e^{(190 / T)}$ |
| B61. $NO_2 + NO_3 \rightarrow NO + NO_2 + O_2$ | 4.5 x $10^{-14}$ x $e^{(-1260 / T)}$ |
| B62. $C_2H_5O_2 + C_2H_5O_2 \rightarrow 2C_2H_5O + O_2$ (0.6), $CH_3CHO + C_2H_5OH + O_2$ (0.4) | 6.8 x $10^{-14}$ x $e^{(-300 / T)}$ |
| B63. $SO_2 + NO_3 \rightarrow$ Products | 7 x $10^{-21}$ |
| B64. $C_2H_5O_2 + HO_2 \rightarrow C_2H_5OOH + O_2$ | 7.5 x $10^{-13}$ x $e^{(700 / T)}$ |
| B65. $C_2H_5O_2 + CH_3O_2 \rightarrow C_2H_5O + CH_3O + O_2$ ($\rightarrow CH_3CHO + HCHO + 2HO_2$) | 0.53x2x(k62x(k25+k60))$^{0.5}$ |
| B66. OH + Alkanes $\rightarrow C_2H_5 + H_2O$ | 1.1 x $10^{-11}$ x $e^{(-1100 / T)}$ |
| B67. $C_2H_5O_2 + NO \rightarrow NO_2 + C_2H_5O$ | 2.6 x $10^{-12}$ x $e^{(365 / T)}$ |
| B68. $CH_3CHO + NO_3 \rightarrow HNO_3 + CH_3CO$ ($\rightarrow CH_3C(O)O_2$) | 1.4 x $10^{-12}$ x $e^{(-1900 / T)}$ |
| B69. $CH_3CHO + O(^3P) \rightarrow OH + CH_3CO$ ($\rightarrow CH_3C(O)O_2$) | 1.8 x $10^{-11}$ x $e^{(-1100 / T)}$ |
| B70. $CH_3CHO + OH \rightarrow H_2O + CH_3CO$ ($\rightarrow CH_3C(O)O_2$) | 5.6 x $10^{-12}$ x $e^{(270 / T)}$ |
| B71. $O(^3P) + H_2S \rightarrow OH + SH$ | 9.2 x $10^{-12}$ x $e^{(-1800 / T)}$ |
| B72. $HO_2 + H \rightarrow H_2O + O$ | 0.02 x 8.1 x $10^{-11}$ |
| B73. $HO_2 + H \rightarrow H_2 + O_2$ | 0.08 x 8.1 x $10^{-11}$ |
| B74. $O(^3P) + H_2 \rightarrow OH + H$ | 4.11 x $10^{-18}$ |
| B75. $NO + CH_3C(O)O_2 \rightarrow NO_2 + CH_3 + CO_2$ | 5.3 x $10^{-12}$ x $e^{(360 / T)}$ |
| B76. $OH + C_2H_5OOH \rightarrow C_2H_4OOH + H_2O$ | 3.64 x $10^{-12}$ |
| B77. $OH + C_2H_5OOH \rightarrow C_2H_5O_2 + H_2O$ | 5.95 x $10^{-12}$ |
| B78. $NO_2 + O(^3P) \rightarrow NO + O_2$ | 6.5 x $10^{-12}$ x $e^{(120 / T)}$ |
| B79. $NO_3 + O(^3P) \rightarrow NO_2 + O_2$ | 1 x $10^{-11}$ |
| B80. $HNO_3 + O(^3P) \rightarrow NO_3 + OH$ | 3 x $10^{-17}$ |
| B81. $C_2H_5O + O_2 \rightarrow CH_3CHO + HO_2$ | 6.3 x $10^{-14}$ x $e^{(-550 / T)}$ |
| B82. $HO_2CH_2O \rightarrow HO_2 + CH_2O$ | 2.4 x $10^{12}$ x $e^{(-7000 / T)}$ |
| B83. $HO_2CH2O + HO_2 \rightarrow HCOOH + O_2 + H_2O$ | 5.6 x $10^{-15}$ x $e^{(2300 / T)}$ |
| B84. $I_2 + O_3 \rightarrow IO + I + O_2$ | 3.8 x $10^{-18}$ |
| B85. $I_2 + O_3 \rightarrow OIO + IO$ | 3.8 x $10^{-18}$ |
| B86. $I + O_3 \rightarrow IO + O_2$ | 2 x $10^{-11}$ x $e^{(-890 / T)}$ |
| B87. $I + HO_2 \rightarrow HI + O_2$ | 1.5 x $10^{-11}$ x $e^{(-1190 / T)}$ |
| B88. $IO + NO \rightarrow I + NO_2$ | 7.3 x $10^{-12}$ x $e^{(330 / T)}$ |
| B89. $IO + HO_2 \rightarrow HOI + O_2$ | 5.8 x $10^{-11}$ |
| B90. $IO + IO \rightarrow OIO + I / I_2O_2$ | 8.6 x $10^{-11}$ |
| B91. $IO + OIO \rightarrow I2O3$ | 1.5 x $10^{-10}$ |
| B92. $OIO + OIO \rightarrow I_2O_4$ | 1 x $10^{-10}$ |
| B93. $IONO_2 \rightarrow IO + NO_2$ | 2.07 x $10^{15}$ x $e^{(-11859 / T)}$ |
| B94. $OIO + NO \rightarrow IO + NO_2$ | 6.7 x $10^{-12}$ |
| B95. $I_2O_2 + O_3 \rightarrow I_2O_3 + O_2$ | 1 x $10^{-12}$ |
| B96. $I_2O_2 \rightarrow OIO + I$ | 0.21 $s^{-1}$ |
| B97. $I_2O_2 \rightarrow IO + IO$ | 1.3 x $10^{-4}$ $s^{-1}$ |
| B98. $I_2O_3 + O_3 \rightarrow I_2O_4 + O_2$ | 1 x $10^{-12}$ |
| B99. $I_2O_4 + O_3 \rightarrow I_2O_5 + O_2$ | 1 x $10^{-12}$ |
| B100. $I_2O_4 \rightarrow 2OIO$ | 4.4 x $10^{-4}$ $s^{-1}$ |
| B101. $I_2 + OH \rightarrow HOI + I$ | 2.1 x $10^{-10}$ |
| B102. $I_2 + NO_3 \rightarrow IO + INO_2$ | 1.5 x $10^{-12}$ |
| B103. $I + NO_3 \rightarrow IO + NO_2$ | 4.5 x $10^{-10}$ |
| B104. $OH + HI \rightarrow I + H_2O$ | 3 x $10^{-11}$ |
| B105. $HOI + OH \rightarrow IO + H_2O$ | 2 x $10^{-13}$ |
| B106. IO + DMS $\rightarrow$ Products | 1.2 x $10^{-14}$ |
| B107. $INO_2 \rightarrow I + NO_2$ | (2.4/0.005) x 2.07x$10^{15}$x$e^{(-11859/T)}$ |
| B108. $Br + O_3 \rightarrow BrO + O_2$ | 1.7 x $10^{-11}$ x $e^{(-800 / T)}$ |

| | |
|---|---|
| B109. $OH + HBr \rightarrow Br + H_2O$ | $1.1 \times 10^{-11}$ |
| B110. $Br + HO_2 \rightarrow HBr + O_2$ | $1.5 \times 10^{-11} \times e^{(-600 / T)}$ |
| B111. $Br + HCHO \rightarrow HBr + HCO$ | $7.7 \times 10^{-12} \times e^{(580 / T)}$ |
| B112. $Br + CH_3CHO \rightarrow HBr + CH_3CO$ | $1.8 \times 10^{-11} \times e^{(-460 / T)}$ |
| B113. $BrO + HO_2 \rightarrow HOBr + O_2$ | $3.4 \times 10^{-12} \times e^{(545/ T)}$ |
| B114. $BrO + NO \rightarrow Br + NO_2$ | $8.8 \times 10^{-12} \times e^{(260/ T)}$ |
| B115. $BrO + DMS \rightarrow Br + DMSO$ | $1.5 \times 10^{-14} \times e^{(850/ T)}$ |
| B116. $BrO + BrO \rightarrow 2Br + O_2$ | $2.4 \times 10^{-12} \times e^{(40/ T)}$ |
| B117. $BrO + BrO \rightarrow Br_2 + O_2$ | $2.8 \times 10^{-14} \times e^{(860/ T)}$ |
| B118. $BrNO_3 \rightarrow BrO + NO_2$ | $2.8 \times 10^{13} \times e^{(-12360/ T)}$ |
| B119. $BrO + IO \rightarrow Br + I + O_2$ (0.3) | $1.5 \times 10^{-11} \times e^{(510/ T)}$ |
| B120. $BrO + IO \rightarrow Br + OIO$ (0.7) | $1.5 \times 10^{-11} \times e^{(510/ T)}$ |
| B121. $Br_2 + OH \rightarrow HOBr + Br$ | $1.9 \times 10^{-11} \times e^{(240/ T)}$ |
| B122. $BrO + OH \rightarrow$ Products | $1.65 \times 10^{-11} \times e^{(-250/ T)}$ |
| B123. $OH + DMS (+ O_2) \rightarrow CH_3SCH_2O_2 + H_2O$ | $9.6 \times 10^{-12} \times e^{(-234 / T)}$ |
| B124. $OH + DMS \rightarrow DMS.OH$ | $(T \times e^{(-234/T)} + 8.46 \times 10^{-10} \times e^{(7230/T)} + 2.68 \times 10^{-10} \times e^{(7810/T)}) / (1.04 \times 10^{11} \times T + 88.1 \times e^{(7460/T)})$ |
| B125. $NO_3 + DMS (+ O_2) \rightarrow CH_3SCH_2O_2 + HNO_3$ | $1.9 \times 10^{-13} \times e^{(520 / T)}$ |
| B126. $CH_3S + O_3 \rightarrow CH_3SO + O2$ | $1.98 \times 10^{-12} \times e^{(290 / T)}$ |
| B127. $CH_3S + NO_2 \rightarrow CH_3SO + NO$ | $2.06 \times 10^{-11} \times e^{(320 / T)}$ |
| B128. $CH_3SO + O_3 \rightarrow CH_3SO_2 + O_2$ | $6 \times 10^{-13}$ |
| B129. $CH_3SO + NO_2 \rightarrow CH_3SO_2 + NO$ | $1.2 \times 10^{-11}$ |
| B130. $CH_3SO_2 + M \rightarrow CH_3 + SO_2 + M$ | $5 \times 10^{13} \times e^{(-(17.2 \times 41840000+RT)/(RT))}$ |
| B131. $CH_3SO_2 + O_3 \rightarrow CH_3SO_3 + O_2$ | $3 \times 10^{-13}$ |
| B132. $CH_3SO_2 + NO_2 \rightarrow CH_3SO_3 + NO$ | $4 \times 10^{-12}$ |
| B133. $CH_3SO_3 + M \rightarrow CH_3 + SO_3 + M$ | $5 \times 10^{13} \times e^{(-(22 \times 41840000+RT)/(RT))}$ |
| B134. $CH_3SO_3 + CH_2O \rightarrow CH_3SO_3H + CHO$ | $1.6 \times 10^{-15}$ |
| B135. $CH_3SO_3 + HO_2 \rightarrow CH_3SO_3H + O_2$ | $5 \times 10^{-11}$ |
| B136. $CH_3S(O)_xOO + NO \rightarrow CH_3S(O)_xO + NO_2$ | $2.4 \times 10^{-11}$ |
| B137. $CH_3S(O)_x + O_2 \rightarrow CH_3S(O)_xOO$ | $1.7 \times 10^{-16} \times e^{(1510 / T)}$ |
| B138. $CH_3S(O)_xOO \rightarrow CH_3S(O)_x + O_2$ | $1.8 \times 10^{11} \times e^{(-3950 / T)}$ |
| B139. $CH_3S(O_2)OO + NO_2 \rightarrow CH_3S(O_2)OONO_2$ | $4.7 \times 10^{-12}$ |
| B140. $CH_3S(O_2)OONO_2 \rightarrow CH_3S(O_2)OO + NO_2$ | $1.9 \times 10^{16} \times e^{(-13543 / T)}$ |
| B141. $CH_3S(O_2)OONO_2 \rightarrow CH_3SO_3H$ (MSA) | $5 \times 10^{-5}$ |
| B142. $CH_3SO_3 + NO_2 \rightarrow CH_3SO_3NO_2$ | $4.7 \times 10^{-12}$ |
| B143. $CH_3SO_3NO_2 \rightarrow CH_3SO_3 + NO_2$ | $1.9 \times 10^{16} \times e^{(-13543 / T)}$ |
| B144. $CH_3SO_3NO_2 \rightarrow CH_3SO_3H$ (MSA) | $5 \times 10^{-5}$ |
| B145. $OH + DMSO \rightarrow DMSO_2 + HO_2$ | $5.8 \times 10^{-11}$ |
| B146. $OH + DMSO_2 \rightarrow CH_3SO_2CH_2O_2$ | $1 \times 10^{-12}$ |
| B147. $CH_3SO_2CH_2O_2 + NO \rightarrow CH_3SO_2 + HCHO + NO_2$ | $4.1 \times 10^{-12} \times e^{(180 / T)}$ |
| B148. $CH_3SO_2CH_2O_2 + HO_2 \rightarrow CH_3SO_2CH_2OOH$ | $1.5 \times 10^{-13} \times e^{(1250 / T)}$ |
| B149. $CH_3SO_2CH_2O_2 + CH_3O_2 \rightarrow CH_3SO_2 + HCHO + CH_3O$ | $3 \times 10^{-13}$ |
| B150. $OH + CH_3SO_2CH_2OOH \rightarrow CH_3SO_2CH_2O_2$ | $1.5 \times 10^{-11}$ |
| B151. $CH_3SCH_2O_2 + NO_3 \rightarrow CH_3S + NO_2 + O_2 + HCHO$ | $2 \times 10^{-12}$ |
| B152. $CH_3SCH_2O_2 + HO_2 \rightarrow CH_3SCH_2OOH$ | $1.5 \times 10^{-13} \times e^{(1250 / T)}$ |
| B153. $CH_3SCH_2O_2 + CH_3O_2 \rightarrow CH_3S + CH_3O + HCHO$ | $3.0 \times 10^{-13}$ |
| B154. $DMDS + OH \rightarrow CH_3SOH + CH_3S$ | $6 \times 10^{-11} \times e^{(400 / T)}$ |
| B155. $DMDS + NO_3 \rightarrow CH_3SO + CH_3S + NO_2$ | $1.3 \times 10^{-12} \times e^{(-270 / T)}$ |
| B156. $CH_3SOH + OH \rightarrow CH_3SO + H_2O$ | $1.1 \times 10^{-10}$ |
| B157. $CH_3SOH + NO_3 \rightarrow CH_3SO + HNO_3$ | $3.4 \times 10^{-12}$ |
| B158. $SH + O_3 \rightarrow SO_2 + OH$ | $9 \times 10^{-12} \times e^{(-280 / T)}$ |
| B159. $CH_3S + CH_3S \rightarrow DMDS$ | $4.15 \times 10^{-11}$ |
| B160. $HSO_3 + O_2 \rightarrow SO_3 + HO_2$ | $1 \times 10^{-11}$ |
| B161. $SO_3 + H_2O \rightarrow H_2SO_4$ | $1.2 \times 10^{-15}$ |
| B162. $NO_3 + CH_3O_2 \rightarrow NO_2 + CH_3O + O_2$ | $1 \times 10^{-12}$ |
| B163. $CH_3C(O)O_2 + CH_3C(O)O_2 \rightarrow 2CH_3CO_2 + O_2 \rightarrow 2CH_3O_2 + 2CO_2$ | $2.9 \times 10^{-12} \times e^{(500/T)}$ |
| B164. $CH_3C(O)O_2 + CH_3O_2 \rightarrow\rightarrow CH_3O_2 + HCHO + HO_2$ | $5.1 \times 10^{-12} \times e^{(272/T)} \times 4.4 \times 10^{5} \times e^{(3910/T)}$ |

| **Recombination Reactions and their Reverse Reactions (where calculated from the Equilibrium Constant)** | $n=\{1+(\mathrm{Log}_{10}(k_0 x[M]/k_\infty))^2\}^{-1}$<br>$k=((k_0 x[M]/(1+k_0[M]/k_\infty)) x F_c)$<br>$F_c$=0.6 unless otherwise noted |
|---|---|
| R1. $O(^1D) + N_2\ (+M) \rightarrow N_2O\ (+M)$ | $[M] x 3.5 x 10^{-37} x (T/300)^{-0.6}$ |
| R2. $HO_2 + HO_2\ (+M) \rightarrow H_2O_2\ (+M)$ | $[M] x 1.7 x 10^{-33}\ x e^{(1000 / T)}$ |
| R3. $H + O_2\ (+ M) \rightarrow HO_2\ (+ M)$ | $k_0 = 5.7\ x 10^{-32}\ x (T/300)^{-1.6}$<br>$k_\infty = 7.5 \times 10^{-11}$ |
| R4. $O_2 + O(^3P) \rightarrow O_3$ | $[M] x 6 x 10^{-34}\ x\ (T/300)^{-2.3}$ |
| R5. $NO_2 + OH \rightarrow HNO_3$ | $k_0 = 2.5 \times 10^{-30} \times (T / 300)^{-4.4}$<br>$k_\infty = 1.6 \times 10^{-11} \times (T / 300)^{-1.7}$ |
| R6. $NO + OH\ (+ M) \rightarrow HONO\ (+ M)$ | $k_0 = 7 \times 10^{-31} \times (T/ 300)^{-2.6}$<br>$k_\infty = 1.5 \times 10^{-11} \times (T / 300)^{-0.5}$ |
| R7. $HO_2 + NO_2\ (+ M) \rightarrow HO_2NO_2\ (+ M)$ | $k_0 = 1.8 \times 10^{-31} \times (T / 300)^{-3.2}$<br>$k_\infty = 4.7 \times 10^{-12} \times (T / 300)^{-1.4}$ |
| R8. $HO_2NO_2 \rightarrow HO_2 + NO_2$ | $k_R = k_F / k_{EQ}$<br>$k_R = k_F/(2.1 x 10^{-27} x\ e^{(10900 / T)})$ |
| R9. $O_2 + CH_3\ (+ M) \rightarrow CH_3O_2\ (+ M)$ | $k_0 = 4.5 \times 10^{-31} \times (T / 300)^{-3}$<br>$k_\infty = 1.8 \times 10^{-12} \times (T / 300)^{-1.7}$ |
| R10. $NO_2 + NO_3\ (+ M) \rightarrow N_2O_5\ (+ M)$ | $k_0 = 2.2 \times 10^{-30} \times (T / 300)^{-3.9}$<br>$k_\infty = 1.5 \times 10^{-12} \times (T / 300)^{-0.7}$ |
| R11. $N_2O_5\ (+ N_2) \rightarrow NO_2 + NO_3\ (+ N_2)$ | $k_R = k_F / k_{EQ}$<br>$k_R = k_F/(2.7 x 10^{-27} x\ e^{(11000 / T)})$ |
| R12. $OH + OH\ (+ M) \rightarrow H_2O_2\ (+ M)$ | $k_0 = 6.2 \times 10^{-31} \times (T / 300)^{-1}$<br>$k_\infty = 2.6 \times 10^{-11}$ |
| R13. $NO + O(^3P)\ (+ M) \rightarrow NO_2\ (+ M)$ | $k_0 = 9 \times 10^{-32} \times (T / 300)^{-1.5}$<br>$k_\infty = 3 \times 10^{-11}$ |
| R14. $NO_2 + O(^3P)\ (+ M) \rightarrow NO_3\ (+ M)$ | $k_0 = 9 \times 10^{-32} \times (T / 300)^{-2}$<br>$k_\infty = 2.2 \times 10^{-11}$ |
| R15. $SO_2 + OH\ (+ M) \rightarrow HOSO_2\ (+ M)$ | $k_0 = 3 \times 10^{-31} \times (T / 300)^{-3.3}$<br>$k_\infty = 1.5 \times 10^{-12}$ |
| R16. $CH_3C(O)O_2 + NO_2\ (+ M) \rightarrow PAN\ (+ M)$ | $k_0 = 9.7 \times 10^{-29} \times (T / 300)^{-5.6}$<br>$k_\infty = 9.3 \times 10^{-12} \times (T / 300)^{-1.5}$ |
| R17. $PAN\ (+ M) \rightarrow CH_3C(O)O_2 + NO_2\ (+ M)$ | $k_R = k_F / k_{EQ}$<br>$k_R = k_F / (9 \times 10^{-29} \times e^{(14000 / T)})$ |
| R18. $OH + Alkenes\ (+ M) \rightarrow HOCH_2CH_2\ (+ M)$ | $k_0 = 1.5 \times 10^{-28} \times (T / 300)^{-0.8}$<br>$k_\infty = 8.8 \times 10^{-12}$ |
| R19. $C_2H_5 + O_2\ (+ M) \rightarrow C_2H_5O_2\ (+ M)$ | $k_0 = 1.5 \times 10^{-28} \times (T / 300)^{-3.8}$<br>$k_\infty = 8 \times 10^{-12}$ |
| R20. $NO_2 + CH_3O_2\ (+ M) \rightarrow CH_3O_2NO_2\ (+ M)$ | $k_0 = 1.5 \times 10^{-30} \times (T / 300)^{-4}$<br>$k_\infty = 6.5 \times 10^{-12} \times (T / 300)^{-2}$ |
| R21. $CH_3O_2NO_2 \rightarrow CH_3O_2 + NO_2$ | $k_R = k_F / k_{EQ}$<br>$k_R=k_F/(1.3 x 10^{-28} x e^{(11200 / T)})$ |
| R22. $I + NO_2\ (+ M) \rightarrow INO_2\ (+ M)$ | $k_0 = 3 \times 10^{-31} \times (T / 300)^{-1}$<br>$k_\infty = 6.6 \times 10^{-11}$<br>$F_c = e^{(-T / 650)} + e^{(-2600 / T)}$ |
| R23. $IO + NO_2\ (+ M) \rightarrow IONO_2\ (+ M)$ | $k_0 = 7.7 \times 10^{-31} \times (T / 300)^{-5}$<br>$k\infty = 1.6 \times 10^{-11}$<br>$F_c = 0.4$ |
| R24. $BrO + NO_2\ (+ M) \rightarrow BrONO_2\ (+ M)$ | $k_0 = 4.7 \times 10^{-31} \times (T / 300)^{-3.1}$<br>$k_\infty = 1.8 \times 10^{-11}$<br>$F_c = 0.4$ |
| R25. $Br + NO_2\ (+ M) \rightarrow BrNO_2\ (+ M)$ | $k_0 = 4.2 \times 10^{-31} \times (T / 300)^{-2.4}$<br>$k_\infty = 2.7 \times 10^{-11} \times (T / 300)^{-0}$<br>$F_c = 0.55$ |
| **Heterogeneous uptake on aerosol** | **Uptake coefficient** |
| H1. $HI \rightarrow 0.5\ I_2$ | 0.1 |
| H2. $HOI \rightarrow 0.5\ IBr + 0.5\ ICl$ | Varied. Base value of 0.1 |
| H3. $IONO_2 \rightarrow 0.5\ IBr + 0.5\ ICl$ | 0.01 |
| H4. $HOBr \rightarrow 0.5\ Br_2$ | 0.1 |
| H5. $HBr \rightarrow 0.5\ Br_2$ | 0.03 |
| H6. $BrNO_3 \rightarrow 0.5\ Br_2$ | 0.1 |

| | |
|---|---|
| H7. $N_2O_5$ → products | 0.08 |
| H8. $NO_3$ → products | 0.03 |
| H9. OH → products | $0.000012 \times e^{(1750 / T)}$ |
| H10. $HO_2$ → products | $0.000000014 \times e^{(3780 / T)}$ |
| H11. $CH_3O_2$ → products | 0.004 |
| H12. $HNO_3$ → products | 0.014 |
| H13. $H_2SO_4$ → products | 0.4 |
| **Photolysis reactions** | Photolysis rates calculated online from absorption cross-sections and quantum yields reported in the relevant reference |
| J1. $O_3 + hv \rightarrow O_2 + O(^1D)$ | |
| J2. $H_2O_2 + hv \rightarrow 2OH$ | |
| J3. $HNO_3 + hv \rightarrow OH + NO_2$ | |
| J4. $HO_2NO_2 + hv \rightarrow OH + NO_3$ | |
| J5. $HONO + hv \rightarrow OH + NO$ | |
| J6. $CH_3OOH + hv \rightarrow CH_3O + OH$ | |
| J7. $CH_2O + hv \rightarrow HCO + H$ | |
| J8. $CH_2O + hv \rightarrow CO + H_2$ | |
| J9. $NO_2 + hv \rightarrow NO + O$ | |
| J10. $NO_3 + hv \rightarrow NO_2 + O$ | |
| J11. $N_2O_5 + hv \rightarrow NO_2 + NO_3$ | |
| J12. $C_2H_5O_2H + hv \rightarrow OH + C_2H_5O$ | |
| J13. $CH_3CHO + hv \rightarrow CH_3 + HCO$ | |
| J14. PAN ($CH_3C(O)O_2NO_2$) $+ hv \rightarrow CH_3C(O)O_2 + NO_2$ | |
| J15. $NO_3 + hv \rightarrow NO + O_2$ | |
| J16. $CH_3I + hv \rightarrow CH_3 + I$ | |
| J17. $CH_2I_2 + hv \rightarrow CH_2I + I \rightarrow CH_2 + 2I$ | |
| J18. $CH_2IBr + hv \rightarrow CH_2Br + I$ | |
| J19. $I_2 + hv \rightarrow 2I$ | |
| J20. $INO_2 + hv \rightarrow I + NO_2$ / $IO + NO$ | |
| J21. $IO + hv \rightarrow I + O$ | |
| J22. $OIO + hv \rightarrow I + O_2$ | |
| J23. $IONO_2 + hv \rightarrow I + NO_3$ | |
| J24. $BrO + hv \rightarrow Br + O$ | |

**Table S6.** Representative concentration of the species used in THAMO.

| Species | Observed concentration range in Fleming *et al.* (52) | Concentration used in Mahajan *et al.* (48) | Concentration used in THAMO |
|---|---|---|---|
| CO | 77-149 | 110 | 100 |
| NO | 10-34 | - | 10 |
| $NO_2$ | - | - | 25 |
| HCHO | 1200-2090 | 500 | 500 |
| CH3CHO | - | 970 | 970 |
| DMS | 23-388 | 30 | 30 |
| $SO_2$ | - | - | 100 |
| Alkenes | - | - | 100 |
| Alkanes | - | - | 300 |
| Isoprene | 5-72 | 10 | 200 |
| $CH_4$ | 1785-1925 | 1820 | 1820 |
| $NO_x$ | 63-352 | - | - |
| Benzene | 18-114 | - | - |
| Methanol | 852-1747 | - | - |
| Ethane | - | 925 | - |
| Propane | - | 60 | - |
| Propene | - | 20 | - |

*Note: the units are in pptv except for CO and $CH_4$, which are in ppbv.*

**Table S7.** The setup of THAMO for six different simulations with various conditions.

| **Simulation** | **$I_2$ and HOI** | **IBr and ICl** | **γ of HOI** | **Average $NO_2$ input (pptv)** |
|---|---|---|---|---|
| 1 | Constrained | Produced | 0.1 | 25 |
| 2 | Constrained | Produced | 0.3 | 25 |
| 3 | Constrained | Produced | 0.9 | 25 |
| 4 | Constrained | Produced | 0.3 | 50 |
| 5 | Constrained | Constrained | 0.3 | 25 |
| 6 | Constrained | - | 0.3 | 25 |

## SI References

1. D. E. Heard *et al.*, The North Atlantic Marine Boundary Layer Experiment(NAMBLEX). Overview of the campaign held at Mace Head, Ireland, in summer 2002. *Atmos. Chem. Phys.* **6**, 2241-2272 (2006).
2. C. O'Dowd *et al.*, Do anthropogenic, continental or coastal aerosol sources impact on a marine aerosol signature at Mace Head? *Atmos. Chem. Phys.* **14**, 10687-10704 (2014).
3. T. Jokinen *et al.*, Atmospheric sulphuric acid and neutral cluster measurements using CI-APi-TOF. *Atmos. Chem. Phys.* **12**, 4117-4125 (2012).
4. H. Junninen *et al.*, A high-resolution mass spectrometer to measure atmospheric ion composition. *Atmos. Meas. Tech.* **3**, 1039-1053 (2010).
5. M. Riva *et al.*, Evaluating the performance of five different chemical ionization techniques for detecting gaseous oxygenated organic species. *Atmos. Meas. Tech.* **12**, 2403-2421 (2019).
6. M. J. Lawler *et al.*, HOCl and $Cl_2$ observations in marine air. *Atmos. Chem. Phys.* **11**, 7617-7628 (2011).
7. J. Sanchez, D. J. Tanner, D. Chen, L. G. Huey, N. L. Ng, A new technique for the direct detection of $HO_2$ radicals using bromide chemical ionization mass spectrometry (Br-CIMS): initial characterization. *Atmos. Meas. Tech.* **9**, 3851-3861 (2016).
8. X. He, From the measurement of halogenated species to iodine particle formation. in *Master's Thesis* (University of Helsinki, http://urn.fi/URN:NBN:fi-fe2017112251826) (2017).
9. M. P. Rissanen, J. Mikkilä, S. Iyer, J. Hakala, Multi-scheme chemical ionization inlet (MION) for fast switching of reagent ion chemistry in atmospheric pressure chemical ionization mass spectrometry (CIMS) applications. *Atmos. Meas. Tech.* **12**, 6635-6646 (2019).
10. M. Wang *et al.*, Measurement of iodine species and sulfuric acid using bromide chemical ionization mass spectrometers. *Atmos. Meas. Tech. Discuss.* **2020**, 1-23 (2020).
11. R. J. Chance, M. Shaw, L. Telgmann, M. Baxter, L. J. Carpenter, A comparison of spectrophotometric and denuder based approaches for the determination of gaseous molecular iodine. *Atmos. Meas. Tech.* **3**, 177-185 (2010).
12. K. A. Schwehr, P. H. Santschi, D. Elmore, The dissolved organic iodine species of the isotopic ratio of $^{129}$**I**/$^{127}$**I**: A novel tool for tracing terrestrial organic carbon in the estuarine surface waters of Galveston Bay, Texas. *Limnol. Oceanogr.: Methods* **3**, 326-337 (2005).
13. A. Kürten, L. Rondo, S. Ehrhart, J. Curtius, Calibration of a Chemical ionization mass spectrometer for the measurement of gaseous sulfuric acid. *J. Phys. Chem. A* **116**, 6375-6386 (2012).
14. V. Riffault, Y. Bedjanian, G. Poulet, Kinetic and mechanistic study of the reactions of OH with IBr and HOI. *J. Photochem. Photobiol. A* **176**, 155-161 (2005).
15. M. J. Tang, R. A. Cox, M. Kalberer, Compilation and evaluation of gas phase diffusion coefficients of reactive trace gases in the atmosphere: volume 1. Inorganic compounds. *Atmos. Chem. Phys.* **14**, 9233-9247 (2014).
16. W. Gu, P. Cheng, M. Tang, Compilation and evaluation of gas phase diffusion coefficients of halogenated organic compounds. *R. Soc. open sci.* **5**, 171936 (2018).
17. A. V. Ivanov, S. Trakhtenberg, A. K. Bertram, Y. M. Gershenzon, M. J. Molina, OH, $HO_2$, and ozone gaseous diffusion coefficients. *J. Phys. Chem. A* **111**, 1632-1637 (2007).
18. R. Atkinson *et al.*, Evaluated kinetic and photochemical data for atmospheric chemistry: Volume III &ndash; gas phase reactions of inorganic halogens. *Atmos. Chem. Phys.* **7**, 981-1191 (2007).
19. M. Passananti *et al.*, How well can we predict cluster fragmentation inside a mass spectrometer? *Chem. Commun.* **55**, 5946-5949 (2019).
20. F. D. Lopez-Hilfiker *et al.*, Constraining the sensitivity of iodide adduct chemical ionization mass spectrometry to multifunctional organic molecules using the collision limit and thermodynamic stability of iodide ion adducts. *Atmos. Meas. Tech.* **9**, 1505-1512 (2016).
21. G. W. Caldwell, J. A. Masucci, M. G. Ikonomou, Negative ion chemical ionization mass spectrometry—binding of molecules to bromide and iodide anions. *Organic Mass Spectrometry* **24**, 8-14 (1989).
22. A. A. Viggiano, J. V. Seeley, P. L. Mundis, J. S. Williamson, R. A. Morris, Rate Constants for the Reactions of $XO_3^-(H_2O)_n$ (X = C, HC, and N) and $NO_3^-(HNO_3)_n$ with $H_2SO_4$: Implications for Atmospheric Detection of $H_2SO_4$. *J. Phys. Chem. A* **101**, 8275-8278 (1997).

23. T. A. Halgren, Merck molecular force field. I. Basis, form, scope, parameterization, and performance of MMFF94. *J. Comput. Chem.* **17**, 490-519 (1996).
24. T. A. Halgren, Merck molecular force field. II. MMFF94 van der Waals and electrostatic parameters for intermolecular interactions. *J. Comput. Chem.* **17**, 520-552 (1996).
25. T. A. Halgren, Merck molecular force field. III. Molecular geometries and vibrational frequencies for MMFF94. *J. Comput. Chem.* **17**, 553-586 (1996).
26. T. A. Halgren, R. B. Nachbar, Merck molecular force field. IV. conformational energies and geometries for MMFF94. *J. Comput. Chem.* **17**, 587-615 (1996).
27. D. Feller, The role of databases in support of computational chemistry calculations. *J. Comput. Chem.* **17**, 1571-1586 (1996).
28. M. Frisch *et al.*, *Gaussian~ 09 Revision D. 01* **(Gaussian, Inc., 2009)** (2014).
29. F. Neese, The ORCA program system. *WIREs Comput. Mol. Sci.* **2**, 73-78 (2012).
30. C. Riplinger, F. Neese, An efficient and near linear scaling pair natural orbital based local coupled cluster method. *J. Chem. Phys.* **138**, 034106 (2013).
31. Y. Minenkov, H. Wang, Z. Wang, S. M. Sarathy, L. Cavallo, Heats of formation of medium-sized organic compounds from contemporary electronic structure methods. *J. Chem. Theory Comput.* **13**, 3537-3560 (2017).
32. B. D. Finley, E. S. Saltzman, Observations of $Cl_2$, $Br_2$, and $I_2$ in coastal marine air. *J. Geophys. Res. Atmos.* **113**, D21301 (2008).
33. N. N. Kazantseva, A. Ernepesova, A. Khodjamamedov, O. A. Geldyev, B. S. Krumgalz, Spectrophotometric analysis of iodide oxidation by chlorine in highly mineralized solutions. *Analytica Chimica Acta* **456**, 105-119 (2002).
34. M. S. Gallagher, D. B. King, P. Y. Whung, E. S. Saltzman, Performance of the HPLC/fluorescence $SO_2$ detector during the GASIE instrument intercomparison experiment. *J. Geophys. Res. Atmos.* **102**, 16247-16254 (1997).
35. R. L. Mauldin Iii *et al.*, OH measurements during the First Aerosol Characterization Experiment (ACE 1): Observations and model comparisons. *J. Geophys. Res. Atmos.* **103**, 16713-16729 (1998).
36. D. J. Tanner, F. L. Eisele, Present OH measurement limits and associated uncertainties. *J. Geophys. Res. Atmos.* **100**, 2883-2892 (1995).
37. D. J. Tanner, A. Jefferson, F. L. Eisele, Selected ion chemical ionization mass spectrometric measurement of OH. *J. Geophys. Res. Atmos.* **102**, 6415-6425 (1997).
38. C. A. Cantrell, A. Zimmer, G. S. Tyndall, Absorption cross sections for water vapor from 183 to 193 nm. *Geophys. Res. Lett.* **24**, 2195-2198 (1997).
39. R. L. Mauldin Iii, D. J. Tanner, F. L. Eisele, Measurements of OH during PEM-Tropics A. *J. Geophys. Res. Atmos.* **104**, 5817-5827 (1999).
40. P. F. DeCarlo *et al.*, Field-deployable, high-resolution, time-of-flight aerosol mass spectrometer. *Anal. Chem.* **78**, 8281-8289 (2006).
41. Y. J. Yoon *et al.*, Seasonal characteristics of the physicochemical properties of North Atlantic marine atmospheric aerosols. *J. Geophys. Res. Atmos.* **112**, D04206 (2007).
42. L. Laakso *et al.*, Ion production rate in a boreal forest based on ion, particle and radiation measurements. *Atmos. Chem. Phys.* **4**, 1933-1943 (2004).
43. Q. T. Nguyen, K. H. Kjær, K. I. Kling, T. Boesen, M. Bilde, Impact of fatty acid coating on the CCN activity of sea salt particles. *Tellus B: Chemical and Physical Meteorology* **69**, 1304064 (2017).
44. P. Zieger *et al.*, Revising the hygroscopicity of inorganic sea salt particles. *Nat. Commun.* **8**, 15883 (2017).
45. T. C. O'Connor, S. G. Jennings, C. D. O'Dowd, Highlights of fifty years of atmospheric aerosol research at Mace Head. *Atmos. Res.* **90**, 338-355 (2008).
46. A. Saiz-Lopez *et al.*, On the vertical distribution of boundary layer halogens over coastal Antarctica: implications for $O_3$, $HO_x$, $NO_x$ and the Hg lifetime. *Atmos. Chem. Phys.* **8**, 887-900 (2008).
47. K. A. Read *et al.*, Extensive halogen-mediated ozone destruction over the tropical Atlantic Ocean. *Nature* **453**, 1232-1235 (2008).
48. A. S. Mahajan *et al.*, Measurement and modelling of tropospheric reactive halogen species over the tropical Atlantic Ocean. *Atmos. Chem. Phys.* **10**, 4611-4624 (2010).

49. M. J. Lawler, A. S. Mahajan, A. Saiz-Lopez, E. S. Saltzman, Observations of $I_2$ at a remote marine site. *Atmos. Chem. Phys.* **14**, 2669-2678 (2014).
50. A. Saiz-Lopez *et al.*, Nighttime atmospheric chemistry of iodine. *Atmos. Chem. Phys.* **16**, 15593-15604 (2016).
51. A. Spolaor *et al.*, Canadian Arctic sea ice reconstructed from bromine in the Greenland NEEM ice core. *Scientific Reports* **6**, 33925 (2016).
52. Z. L. Fleming *et al.*, Peroxy radical chemistry and the control of ozone photochemistry at Mace Head, Ireland during the summer of 2002. *Atmos. Chem. Phys.* **6**, 2193-2214 (2006).
53. J. D. Lee *et al.*, Reactive Halogens in the Marine Boundary Layer (RHaMBLe): the tropical North Atlantic experiments. *Atmos. Chem. Phys.* **10**, 1031-1055 (2010).
54. K. A. Read *et al.*, Intra-annual cycles of NMVOC in the tropical marine boundary layer and their use for interpreting seasonal variability in CO. *J. Geophys. Res. Atmos.* **114** (2009).
55. R. J. Huang *et al.*, In situ measurements of molecular iodine in the marine boundary layer: the link to macroalgae and the implications for $O_3$, IO, OIO and $NO_x$. *Atmos. Chem. Phys.* **10**, 4823-4833 (2010).
56. G. McFiggans *et al.*, Direct evidence for coastal iodine particles from Laminaria macroalgae – linkage to emissions of molecular iodine. *Atmos. Chem. Phys.* **4**, 701-713 (2004).
57. A. Saiz-Lopez, R. von Glasow, Reactive halogen chemistry in the troposphere. *Chem. Soc. Rev.* **41**, 6448-6472 (2012).
58. W. R. Simpson, S. S. Brown, A. Saiz-Lopez, J. A. Thornton, R. Glasow, Tropospheric halogen chemistry: sources, cycling, and impacts. *Chem. Rev.* **115**, 4035-4062 (2015).
59. R. P. Fernandez *et al.*, Modeling the Sources and Chemistry of Polar Tropospheric Halogens (Cl, Br, and I) Using the CAM-Chem Global Chemistry-Climate Model. *J. Adv. Model. Earth Syst.* **11**, 2259-2289 (2019).
60. A. Saiz-Lopez, J. M. C. Plane, J. A. Shillito, Bromine oxide in the mid-latitude marine boundary layer. *Geophys. Res. Lett.* **31**, L03111 (2004).
61. G. McFiggans, R. A. Cox, J. C. Mössinger, B. J. Allan, J. M. C. Plane, Active chlorine release from marine aerosols: Roles for reactive iodine and nitrogen species. *J. Geophys. Res. Atmos.* **107**, ACH 10-11-ACH 10-13 (2002).
62. M. Ammann *et al.*, Evaluated kinetic and photochemical data for atmospheric chemistry: Volume VI – heterogeneous reactions with liquid substrates. *Atmos. Chem. Phys.* **13**, 8045-8228 (2013).
63. J. C. Mössinger, R. A. Cox, Heterogeneous Reaction of HOI with Sodium Halide Salts. *J. Phys. Chem. A* **105**, 5165-5177 (2001).
64. N. S. Holmes, J. W. Adams, J. N. Crowley, Uptake and reaction of HOI and $IONO_2$ on frozen and dry NaCl/NaBr surfaces and $H_2SO_4$. *Phys. Chem. Chem. Phys.* **3**, 1679-1687 (2001).
65. C. F. Braban *et al.*, Heterogeneous reactions of HOI, ICl and IBr on sea salt and sea salt proxies. *Phys. Chem. Chem. Phys.* **9**, 3136-3148 (2007).
66. G. A. Lugg, Diffusion coefficients of some organic and other vapors in air. *Anal. Chem.* **40**, 1072-1077 (1968).
67. S. P. S. Andrew, A simple method of measuring gaseous diffusion coefficients. *Chem. Eng. Sci.* **4**, 269-272 (1955).
68. S. Fickert, J. W. Adams, J. N. Crowley, Activation of $Br_2$ and BrCl via uptake of HOBr onto aqueous salt solutions. *J. Geophys. Res. Atmos.* **104**, 23719-23727 (1999).